Subsurface weathering signatures in stream chemistry during an intense storm

Jon K. Golla [a,*], Julien Bouchez [b], Marie L. Kuessner [b], Daniella M. Rempe [c], Jennifer L. Druhan [a,b]

[a] *Department of Geology, University of Illinois at Urbana-Champaign, Urbana, 61801, IL, USA*
[b] *Institut de Physique du Globe de Paris, Sorbonne Paris Cité, Université Paris Diderot, CNRS, Paris, 75238, France*
[c] *Jackson School of Geosciences, University of Texas at Austin, Austin, 78712, TX, USA*

ABSTRACT

Long-term relationships between stream chemistry and discharge are regulated by watershed subsurface structure and biogeochemical functioning. The extent to which these mechanisms are expressed and may be explored in the geochemical response of streams during storm events remains an open question. Here, we monitor an intense storm as it infiltrated an upland hillslope draining into a small steep canyon stream that is typified by chemostatic concentration-discharge relationships in rock-derived solutes. Our approach couples a high-frequency record of stable lithium isotope ratios (δ^7Li) in the stream with novel sampling of rock moisture within the hillslope. At peak discharge, lithium-sodium ratios (Li/Na) increased from 0.58 μM/mM to 0.82 μM/mM and δ^7Li decreased from $+28.9 \pm 0.1$‰ to $+26.4 \pm 0.4$‰ in the stream. Hillslope hydrologic monitoring reveals that the rainwater infiltrated the subsurface, yet attenuated breakthrough of the heavily depleted δD signal of this storm (as low as -86‰) only reached the upper 3-4 meters of the vadose zone. These δD data show that the storm water mixed with previously stored rock moisture and displaced stored fluid to deeper depths, causing an observable rise in the water table. Groundwater ^{87}Sr/^{86}Sr and δ^7Li demonstrate consistency in the fluid-rock interactions that occur below the water table prior to and during the storm. In total, these observations indicate that the transfer of fluid and generation of solutes through the interior of the hillslope produce the variability of Li/Na and δ^7Li within the stream during the storm, and support application of a previously established 1-D reactive transport model framework developed for the evolution of lithium within the hillslope to this extreme hydrologic event. Based on the model, both Li/Na and δ^7Li versus discharge relationships reflect an overall shorter transit time of fluid through the interior of the hillslope. These model results are consistent with our hydrologic observations and indicate that Li from further upslope (where the vadose zone becomes thicker) contributes to stream solute chemistry at the height of the storm. We conclude that in this system, stream lithium isotope signatures record the routing of water and generation of solutes within the hillslope even during intense storm events.

1. Introduction

The geochemistry of streamflow offers a unique window into landscape functioning and evolution, as it integrates a range of water ages transiting the biogeochemical reaction network inherent to a given watershed. Basic relationships between solute concentration (C) and discharge (Q) have long been used to infer changes in transport and reaction pathways in the Critical Zone (e.g., Anderson et al., 1997; Arora et al., 2020; Baronas et al., 2017; Basu et al., 2010; Bieroza and Heathwaite, 2015; Chanat et al., 2002; Evans and Davies, 1998; Godsey et al., 2009; Johnson et al., 1969; Miller and Drever, 1977; Knapp et al., 2020; Rose et al., 2018; Torres and Baronas, 2021). Weathering-derived solutes (e.g., Na, K, Mg, Ca, and Si) often display chemostatic behavior or little variability in concentration over a broad range of discharge values (e.g., Diamond and Cohen, 2018; Godsey et al., 2009; Herndon et al., 2015; Koger et al., 2018; Sullivan et al., 2019; Wlostowski et al., 2018). This capacity for solute export to 'keep pace' with discharge has been attributed to a substantial supply of rock-derived solutes that are accessed during flood events (e.g., Basu et al., 2010; Thompson et al., 2011), while others have suggested sufficiently rapid reaction rates such that the timescale of weathering does not lag

behind the timescale of fluid transport (e.g., Ameli et al., 2017; Maher, 2011). Under such conditions, water-rock reactions buffer the chemistry of fluid contributing to streamflow.

Connecting stream solute chemistry to the reactions occurring in hillslopes is challenging. Previous studies have noted that multiple coupled solubilization and secondary mineral formation reactions can result in comparable solute concentrations (e.g., Kim et al., 2017; Torres and Baronas, 2021). Hence, a variety of reactive pathways may contribute both across the heterogeneous structure of the near-surface Critical Zone and over transient fluctuations in infiltration rate and discharge to produce apparently chemostatic behavior. Furthermore, most observations of chemostatic solute signatures in upland watersheds are based on relatively low-frequency monitoring records typically spanning seasonal and annual timescales (e.g., Diamond and Cohen, 2018; Godsey et al., 2009; Herndon et al., 2015; Koger et al., 2018; Sullivan et al., 2019; Wlostowski et al., 2018). As a result, the C-Q relationships inferred from these records often integrate over indiscriminate sampling "snapshots" of systems subject to hydrological and biogeochemical perturbations across a wide range of timescales (e.g., individual storm events, seasonal variation in baseflow).

Individual storm events can generate as much as 80% of annual solute fluxes in small catchments across a variety of climates and lithology (e.g., Inamdar et al., 2006; Lesack, 1993; Petrone et al., 2006; Ryan et al., 2021). Only a limited number of studies have reported data sufficient to compare weathering-derived C-Q patterns across individual storms and systematic monitoring records. Rose et al. (2018) monitored C-Q patterns in 44 individual storms spanning 11 years in White Clay Creek, located in Pennsylvania, USA. They reported consistency between individual storm and long-term behavior, although the latter was compiled from storm events rather than an independent monitoring effort. At the Erlenbach catchment in Switzerland, Knapp et al. (2020) also suggested consistency between base flow and flood C-Q relationships for major elements derived from weathering. In contrast, many interpretations of stream solute chemistry during individual precipitation events utilize mixing models that suggest bypassing of the subsurface below soil during intense infiltration (e.g., Bazemore et al., 1994; Gardner et al., 2017; Kurtz et al., 2011; Mulholland et al., 1990; Schellekens et al., 2004). Hence, it remains unclear to what extent the behavior of weathering-derived solutes during storm events simply falls within the broader C-Q patterns observed over seasonal and annual variations in discharge, or if these events trigger major modifications to the routing of water to the stream and thus the origin and composition of solutes recorded across storm hydrographs. Furthermore, it remains uncertain whether C-Q relationships break down at high discharge rates produced by extreme events, which are presently projected to increase in frequency with intensification of the hydrologic cycle.

Analyses of C-Q patterns and the exploration of the potential underlying factors that yield apparent chemostasis in C-Q relationships of rock-derived solutes are greatly aided by tracers sensitive to the water-rock reaction network producing these solutes. A new generation of highly precise and increasingly routine stable metal(loid) isotope analysis (e.g., B, Li, and Si) now offers heightened sensitivity to the precipitation and dissolution reactions that underlie C-Q patterns (e.g., Burton and Vigier, 2012; Fernandez et al., 2022; Fries et al., 2019; Frings et al., 2021; Gaillardet and Lemarchand, 2018). Among this suite of elements, lithium (Li) and its stable isotopes are an ideal tracer of the fluid-rock weathering reactions that generate rock-derived solutes, due to characteristic mass-dependent fractionation during secondary clay formation (e.g., Huh et al., 2001; Pistiner and Henderson, 2003; Rudnick et al., 2004). Furthermore, Critical Zone Li isotope signatures are simplified relative to many other weathering-derived solutes because of minimal, nominally non-fractionating Li uptake by plants (Lemarc-

hand et al., 2010; Pogge von Strandmann et al., 2014). Furthermore, recent efforts to couple fluid flow paths and fractionating reactions in a forward modeling framework seem to suggest that stable isotope ratios may afford heightened sensitivity to variations in fluid drainage rates and patterns compared to solute concentrations (Druhan and Maher, 2017; Fernandez et al., 2022).

Here, we present a high-frequency record of stable Li isotopes and rock-derived solutes during an intense storm fed by an "atmospheric river" (as defined in Ralph et al., 2018 and DeFlorio et al., 2018) using a heavily instrumented upland hillslope (Rivendell, Eel River Critical Zone Observatory, California, USA) draining into Elder Creek, a steep canyon stream. Prior C-Q analysis of Elder Creek based on the USGS Hydrologic Benchmark Network describes strongly chemostatic behavior in the major rock-derived solutes over three orders of magnitude in discharge (Godsey et al., 2009). Kim et al. (2014, 2017) used groundwater and stream chemistry to argue that water-rock reactions in the vadose zone constitute the principal source of solute flux through this system, although they lacked direct observations of rock moisture above the water table. Subsequent novel instrumentation has allowed unprecedented access to the fluid draining through the interior of the hillslope (Rempe and Dietrich, 2018; Tune et al., 2020). We have previously used the major ion concentrations and Li isotope signatures of these fluids to constrain the silicate weathering reactions that govern solute production and cycling across the vadose zone and through the shallow aquifer in a forward, multi-component numerical reactive transport framework (Golla et al., 2021). From this basis, we now leverage a novel data set of hydrologic monitoring, water isotopes, and Li isotope signatures to uncover sensitivity in the rock-derived solutes of a characteristically chemostatic stream across a storm hydrograph.

2. Materials and methods

2.1. Study area and sampling

The 17-km^2 Elder Creek watershed is located within the Angelo Coast Range Reserve in Mendocino County, California USA as part of the U.S. National Science Foundation Critical Zone Observatory program (Fig. 1). Elder Creek is a relatively steep canyon river, in an actively uplifting landscape, fed by tributaries which are primarily cut by periodic debris flows. We utilize the extensively instrumented Rivendell hillslope (Kim et al., 2014; Rempe and Dietrich, 2018; Salve et al., 2012; Tune et al., 2020). Rivendell consists of thin soil (0.3 - 0.7 m) and thick, fractured weathered argillite (4 - 30 m) (Rempe and Dietrich, 2018; Tune et al., 2020) locally interbedded with sandstone lenses, typifying the Coastal Belt of the Franciscan Complex (McLaughlin et al., 2000). The mineral assemblage of fresh bedrock is comprised of a mixture of primary minerals (quartz, K-feldspar, plagioclase, chlorite) and clays (chlorite, smectite, kaolinite, illite) (Gu et al., 2020; Kim et al., 2014). Active regional uplift and erosion occur at 0.2-0.4 mm/yr (Fuller et al., 2009).

The study area is characterized by a Mediterranean climate (i.e., warm, dry summers and cool, wet winters), where most precipitation is received as rain with an annual mean total of ~2042 mm and temperatures can range from -8 to 32 °C (Kim et al., 2014; Rempe and Dietrich, 2018; Salve et al., 2012). Hydrologic surveying shows that the height of the water table at midslope can vary by as much as 10 m (Rempe and Dietrich, 2018). The thin soil layer and unsaturated weathered bedrock host reactive gases (Tune et al., 2020) and the deep roots of a mixed conifer-hardwood evergreen forest (Oshun et al., 2016; Salve et al., 2012). Runoff to the stream channel is dominated by subsurface flow. Overland flow on the Rivendell hillslope generally does not occur (Salve et al., 2012). However, saturated overland flow (i.e., Dunne overland flow;
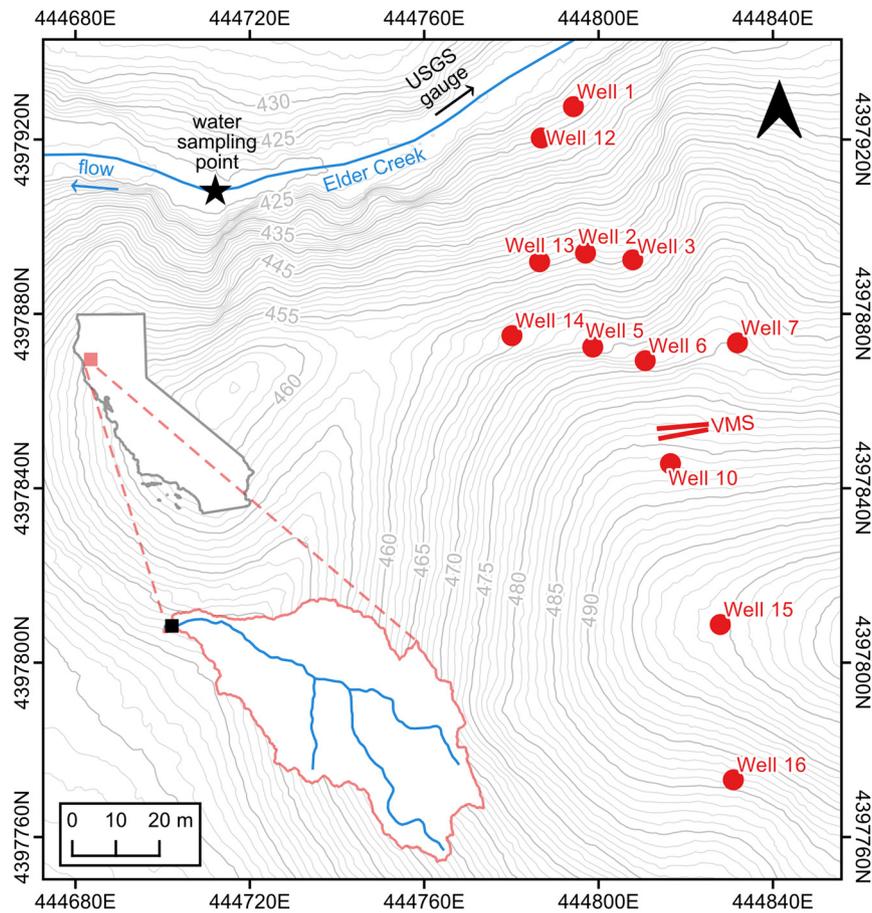
Fig. 1. Map of the Rivendell hillslope showing locations of the groundwater well network (red circles), the Vadose Zone Monitoring System (set of two red solid lines), and Elder Creek sampling (black star) with coordinates in NAD83 / UTM Zone 10N (EPSG:26910). The U.S. Geological Survey stream gauge (#11475560) is upstream of the Elder Creek water sampling collection site. Elevation data are derived from a National Center for Airborne Laser Mapping survey in 2014 (Rempe and Dietrich, 2018). The insets show the relative location of the study area within California, United States and the greater Elder Creek watershed as light red and black squares, respectively. (For interpretation of the colors in the figure(s), the reader is referred to the web version of this article.)

Dunne and Black, 1970a,b) has been observed in topographically convergent areas during intense storms. The storm reported in this study was the result of an atmospheric river that produced runoff as much as ∼34 times greater than the mean annual value. During this period, Elder Creek was sampled for solute chemistry and stable isotope analysis at high frequency from January 5-13, 2017. Groundwater wells distributed across the Rivendell hillslope were sampled within the period of the storm event (January 5-11).

At Rivendell, there is a unique Vadose Zone Monitoring System (VMS), which consists of a pair of instrumented sleeves inserted through subvertical boreholes across ∼16 m of the hillslope (Golla et al., 2021; Tune et al., 2020). Each sleeve is lined with a set of 10 ports approximately 1.5 m apart and equipped with discrete lysimeter samplers to collect waters draining weathered bedrock. In addition, each set of VMS sampling ports is separately capable of collecting gases through perforated tubing and of measuring water content and temperature with time-domain transmission sensors. Among the 20 total ports, the first eight ports from 0.8-6.9 m below land surface are perennially unsaturated, whereas the deepest two ports at 14.7 m and 16.5 m remain fully saturated throughout the year. The ports in between 6.9 m and 14.7 m are seasonally saturated due to fluctuation of the groundwater table elevation. A complete description of the corresponding depths to the VMS sampling apparatus can be found in Tune et al. (2020) and further technical details of the general functioning of the VMS have been outlined by Dahan et al. (2009) and Rimon et al. (2007).

2.2. Hydrological monitoring

Groundwater levels are measured via continuous pressure transducers across a network of 12 wells (Fig. 1). A U.S. Geological Survey gauging station (#11475560) monitors streamflow every 15 minutes and is located approximately 30 m upstream of the collection point for water chemistry. Precipitation data are collected across a network of tipping bucket rain gauges and distributed by the Eel River Critical Zone Observatory (https://dendra.science/). Historical precipitation for the Elder Creek watershed comes from PRISM (Daly et al., 2008, 2015).

Time-domain transmission (TDT) sensors along one of the VMS sleeves provide records of water content and temperature at 15-minute intervals. To approximate time-variable rock moisture storage in the root zone, we use relative moisture contents measured via TDT sensors at 1.95 m, 3.64 m, and 5.22 m depths in the VMS. These three moisture content time series are averaged to create a composite time series for the root zone that is scaled from the minimum dynamic storage (0 mm) to the maximum dynamic rock moisture storage of 280 mm (Rempe and Dietrich, 2018).

To calculate a rate of drainage from the root zone (i.e. vadose zone flux), we establish a time-dependent root-zone water balance, based on our time series of rock moisture storage, precipitation (P), approximate interception (20%; Salve et al., 2012), and evapotranspiration (ET, 1.5 mm/day annual average; PRISM, 2022):

$$D = P - 0.2 * P - ET - \Delta S, \tag{1}$$

where ΔS is the daily change in storage calculated from the composite moisture time series and D is drainage in mm/day.

2.3. Geochemical analyses

All water isotope samples were analyzed at the University of California, Berkeley Center for Stable Isotope Biogeochemistry. Samples were run via Isotope Ratio Mass Spectrometry on a Thermo Delta PLUS XL instrument. Data are reported in standard delta per-mille notation relative to Vienna Standard Mean Ocean Water (VSMOW)

$$\delta D = \left(\frac{\frac{^2H}{^1H} sample}{\frac{^2H}{^1H} VSMOW} - 1 \right) \times 1000, \tag{2}$$

where a similar expression can be written for stable oxygen isotopes (i.e., ^{18}O and ^{16}O). Precision of long-term VSMOW measurements are on the order of $\pm 1.0\permil$ for δD and $\pm 0.11\permil$ for $\delta^{18}O$ (Oshun et al., 2016). These data are available as supplementary material.

The concentrations of cations and anions were measured at the PARI analytical platform of the Institut de Physique du Globe de Paris (IPGP) with an Agilent 7900 quadrupole ICP-MS and a Dionex DX-120 ion chromatograph, respectively. The accuracy of cation concentrations is based on the precision of the percent error ($\leq 5\%$) of repeated measurements of the SLRS-5 river water standard.

Radiogenic strontium (Sr) isotopes were measured at IPGP. Sr purification was performed by ion chromatography using Eichrom Sr-SPEC resin following a method developed by Pin and Bassin (1992) and Sr isotope ratio measurements were made with a Thermo Scientific Neptune MC-ICP-MS following the method outlined in Hajj et al. (2017) (see Supplementary Text S1 for further details).

Lithium isotopes were measured using a Thermo Scientific Neptune MC-ICP-MS at the PARI analytical platform of IPGP HELGES laboratory of the GeoForschungsZentrum (GFZ) German Research Centre for Geosciences. Samples were treated with HF and H_2O_2 to eliminate Si and organic matter and loaded onto columns filled with 4 mL of BioRad AG50-X12 (200-400 mesh) resin for Li purification following the chemical separation protocol of James and Palmer (2000). Prior to introduction into an Elemental Scientific APEX-HydroFlouric desolvating nebulizer, the eluted fraction was evaporated to near-dryness and taken up in 0.5-M HNO_3 to obtain a 20 ng/mL Li solution. Analyses were performed with operating conditions similar to those reported by Millot et al. (2004). Results are expressed in standard delta per-mille notation

$$\delta^7 Li = \left(\frac{\frac{^7Li}{^6Li} sample}{AVG(\frac{^7Li}{^6Li} std-I, \frac{^7Li}{^6Li} std-II)} - 1 \right) \times 1000, \tag{3}$$

where std-I and std-II refer to the L-SVEC Li carbonate standard (Flesch et al., 1973) evaluated directly before and after each sample. The analytical uncertainty for individual samples is reported using a 95% confidence interval

$$95\% CI = t_{n-1} \frac{\sigma}{\sqrt{n}}, \tag{4}$$

where σ is the standard deviation of n replicate measurements of a sample and t_{n-1} is the critical value of a Student's t-distribution over a 95% confidence level. Long-term accuracy of Li isotope analysis is based on repeated measurements ($\overline{x} \pm 2\sigma$) of OSIL Atlantic seawater ($\delta^7 Li = 30.88 \pm 0.76\permil$; n = 4). In addition, we also report measurements of other reference materials for basalt (BHVO-2: 4.77 $\pm 0.09\permil$; JB-2: 4.99 $\pm 0.06\permil$) and soil (TILL-1:

7.21 $\pm 0.27\permil$). The measurements of basalt standards are in agreement with published measurements (Li et al., 2019 and references therein), while the TILL-1 measurement is slightly higher than literature values (Weynell et al., 2017, 2021; Zhang et al., 2021). In the following figures, both the 95% confidence interval calculated from sample replicate measurements (Equation 4) and the 2σ associated to repeated analyses of the OSIL Atlantic seawater reference material are shown as error bars for $\delta^7 Li$.

All data are presented in Table 1. The results of solute chemistry and Li isotope analyses reported in this study were part of the same analytical session as in Golla et al. (2021).

3. Results

3.1. Delivery of storm water to Rivendell and Elder Creek

An intense storm as a result of an atmospheric river occurred on January 5-13, 2017 delivering 416 mm of precipitation (Fig. 2a). Relative to storms between water years 1981 and 2018, 2017 storm was in the 95th percentile of storm intensity and the 89th percentile of total storm precipitation (Fig. S1). Across the same period, this storm was the 12th most intense storm on record (57 mm/hr) relative to an average value of 33 mm/hr (Fig. S1). The 2017 water year was relatively wet, amounting to 3375 mm of total rainfall (Fig. 2a), which is ~65% more than the annual average (Rempe and Dietrich, 2018).

Every year, vadose zone storage increases with the infiltration of the first rains of the wet season and vadose zone water storage decreases progressively over the dry, growing season. In 2017, the atmospheric river arrived after vadose zone storage had approached field capacity (Fig. 2b), defined as the maximum water content held in tension by soil and unsaturated weathered bedrock once drainage has ceased following infiltration. No overland flow was observed in the location of the VMS, meaning that this storm triggered transport through the vadose zone as opposed to an increase in water storage. The vadose zone water flux was higher for this event relative to other storms in water year 2017 (Fig. 2b) and peaked at 142 mm/day, which is 14 times the average wet season vadose zone water flux. Such resolution of water storage in and flux through a partially saturated bedrock vadose zone is rare and typically difficult to quantify, and is only afforded in this study by the unique VMS instrumentation (subsection 2.1; Tune et al., 2020).

During the storm, groundwater levels observed in the wells rose (Fig. S2), despite the fact that the water table was already high in the midst of the wet season. This small but detectable change led to an increase in the hillslope hydraulic gradient ($\frac{\Delta H}{\Delta x}$) (Fig. 2c) and thus, groundwater flux (Fig. 2c). During the storm, $\frac{\Delta H}{\Delta x}$ increased between Wells 12 and 6 by 5% (bracketed by dashed lines in Fig. 2c). Assuming a constant hydraulic conductivity, we infer that the groundwater flux increased by 5% between the start and peak of the storm. Hence, we observe a concurrent increase in fluid flux across both the bedrock vadose zone and the laterally draining groundwater as a result of this intense storm event.

This groundwater flow rate was the highest recorded for the season and roughly coincident with annual peak runoff (95th percentile) in Elder Creek (Fig. S1). Relative to other water years from 1968 to 2020, the peak Elder Creek discharge produced by this intense storm is in the 79th percentile of annual peak discharge values. In the Elder Creek watershed, the majority of runoff occurs during storm events (Salve et al., 2012). For example, in this relatively wet 2017 water year, the 8-day storm event constituted about 14% of the total annual volume of water discharged by Elder Creek. Long-term physical monitoring of groundwater and vadose zone storage at the site indicates that Elder Creek runoff is nearly entirely derived from groundwater. Overland flow and lateral flow

Table 1

Elemental concentrations and isotopic compositions of Elder Creek, groundwaters, and digested solid samples. Groundwater sample names include the corresponding wellhead elevation. Samples annotated with an asterisk (*) have been previously reported in (Golla et al., 2021) for cation and SiO$_2$ concentrations and δ^7Li values. Stream discharge values for Elder Creek samples are estimated as the nearest measurement in the 15-minute resolution data set from the U.S. Geological Survey gauging station #11475560. The 2σ associated to isotope measurements are based on a set of triplicate measurements. The analytical precision associated with elemental concentrations is typically $\leq$5% based on long-term measurements of the river water reference material SLRS-5 (National Research Council, Canada). The accuracy of Li isotope analyses can be assessed from the sample-specific 2σ of replicate measurements tabulated below and from the 2σ of repeated analyses of the OSIL Atlantic seawater reference material ($\pm$0.76‰; n = 4).

Sample	Date	Time	Discharge (m^3/s)	Na	K	Ca	Mg	SiO$_2$	Cl	SO$_4$	HCO$_3$	Sr	^{87}Sr/^{86}Sr	2$\sigma \times 10^{-6}$	Li	δ^7Li (‰)	2σ ‰
							μmol/L (fluid samples) and mmol/kg (solid samples)										
Elder Creek*	2017-01-05	17:30	1.7	251	14	247	136	239	59	15	949	1.12	0.709770	22	0.120	28.30	0.14
Elder Creek	2017-01-06	7:50	1.5	248	14	247	136	240	60	15	957	1.14			0.122		
Elder Creek	2017-01-06	17:30	1.4	253	14	253	140	238	63	17	992	1.17			0.122		
Elder Creek	2017-01-06	23:12	1.4	251	16	251	138	241	63	17	979	1.19			0.122		
Elder Creek*	2017-01-07	5:20	1.4	246	14	247	136	234	62	17	959	1.24	0.709770	26	0.119	28.90	0.15
Elder Creek	2017-01-07	10:42	1.7	159	9	157	86	222	59	17	908	0.76			0.082		
Elder Creek*	2017-01-07	13:46	1.9	226	13	217	120	219	54	15	903	0.99	0.709770	25	0.114	28.68	0.14
Elder Creek	2017-01-07	15:10	2.1	232	14	224	123	214	54	14	893	1.02			0.111		
Elder Creek*	2017-01-07	16:57	2.0	230	14	222	122	216	53	15	877	0.99	0.709770	26	0.111	28.61	0.11
Elder Creek	2017-01-07	23:26	1.9	235	14	229	126	224	56	16	919	1.03			0.116		
Elder Creek*	2017-01-08	5:40	2.4	229	14	220	120	214	56	14	871	0.94	0.709770	25	0.118	28.30	0.21
Elder Creek	2017-01-08	10:40	4.4	237	16	222	121	189	44	12	767	0.98	0.709771	25	0.156		
Elder Creek	2017-01-08	13:40	8.3	162	13	146	80	152	32	8	590	0.61			0.092		
Elder Creek	2017-01-08	16:07	9.3	167	14	148	82	164	34	8	622	0.63			0.093		
Elder Creek	2017-01-08	19:10	8.9	160	11	116	64	183	41	10	687	0.45	0.709771	25	0.099	27.45	0.34
Elder Creek	2017-01-08	23:20	8.3	181	14	162	89	197	41	10	717	0.64			0.106		
Elder Creek	2017-01-09	5:20	7.1	190	14	172	95	213	49	11	752	0.68			0.118		
Elder Creek	2017-01-09	8:30	6.6	210	14	174	97	222	48	10	758	0.70			0.119		
Elder Creek	2017-01-09	11:30	6.2	209	15	186	104	222	52	15	785	0.74	0.709772	27	0.122	27.08	0.29
Elder Creek	2017-01-09	14:45	5.9	204	14	178	99	225	52	10	757	0.71			0.120		
Elder Creek	2017-01-09	17:30	5.6	210	15	188	105	227	53	11	771	0.76			0.123		
Elder Creek	2017-01-09	20:35	5.7	193	13	165	92	223	52	11	777	0.64			0.124		
Elder Creek	2017-01-09	23:30	6.2	204	14	182	102	215	49	11	765	0.71	0.709773	28	0.123	26.74	0.28
Elder Creek	2017-01-10	5:30	7.4	197	14	174	97	210	52	11	723	0.71			0.116		
Elder Creek	2017-01-10	8:15	8.3	188	15	162	90	197	47	9	679	0.63	0.709772	26	0.107	26.53	0.32
Elder Creek	2017-01-10	11:27	14.7	169	15	144	80	178	38	8	610	0.58			0.095		
Elder Creek	2017-01-10	14:35	25.1	150	18	133	72	168	37	7	534	0.60			0.086		
Elder Creek	2017-01-10	17:30	29.4	151	19	132	72	175	38	8	557	0.59			0.082	26.37	0.45
Elder Creek	2017-01-10	20:45	23.7	159	18	139	77	186	46	8	572	0.60			0.088		
Elder Creek	2017-01-10	23:20	23.9	165	18	143	78	189	46	8	598	0.63			0.089		
Elder Creek	2017-01-11	5:31	13.8	188	17	153	86	213	47	8	709	0.62			0.104		
Elder Creek	2017-01-11	8:57	10.0	203	16	156	88	224	49	9	701	0.65			0.112		
Elder Creek	2017-01-11	11:25	8.5	180	16	164	90	218	50	9	691	0.71	0.709773	31	0.108	26.56	0.36
Elder Creek	2017-01-11	14:10	8.1	184	15	159	89	222	52	10	722	0.76			0.112		
Elder Creek	2017-01-11	17:45	7.7	185	15	165	92	230	54	10	715	0.75			0.115		
Elder Creek	2017-01-11	19:58	7.2	182	15	160	89	242	51	10	736	0.74			0.116		
Elder Creek	2017-01-11	23:36	6.8	198	16	181	101	246	51	9	736	0.84			0.118		
Elder Creek	2017-01-12	8:45	6.0	194	14	177	99	253	52	10	760	0.83	0.709773	25	0.123	26.68	0.46
Well 2 (420 m)	2017-01-11	12:38					234	252				1.67			0.588	22.10	0.29
Well 5* (449 m)	2017-01-06	9:53					353	219				13.73	0.709774	28	0.825		
Well 5 (449 m)	2017-01-11	11:35					116	247				0.45	0.709774	27	0.534		
Well 7 (454 m)	2017-01-11	11:16					52	235				0.31			0.221	10.55	0.22
Well 10*	2017-01-06	11:40					78	287				0.18	0.709774	30	0.576	15.66	0.30
Well 10	2017-01-11	10:55					37	240				0.19	0.709776	45	0.172	13.57	0.15
Well 12* (402 m)	2017-01-05	13:40					463	189				9.66	0.709774	24	0.577	23.74	0.37
Well 12 (402 m)	2017-01-11	12:15											0.709774	24	0.371	24.35	0.24
Well 13* (420 m)	2017-01-05	15:25					518	135				4.07	0.709776	23	0.398		
Well 13 (420 m)	2017-01-11	12:53					552	141				3.89	0.709776	24	0.392		
Well 15 (468 m)	2017-01-11	10:16					103	316				0.52			0.363	16.01	0.21
Bedrock*	2017-01-08			729	627		739					1.96	0.709838	25	7.76	−0.57	0.18
Stream sediment	2017-01-08			910	611		827					0.81	0.709792	26			
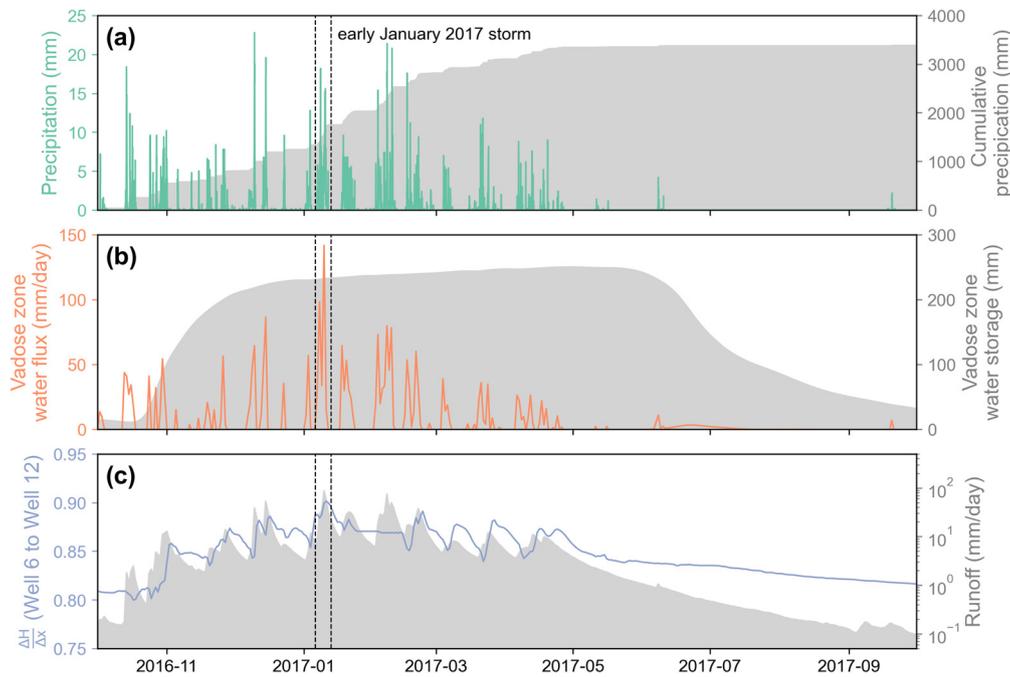
Fig. 2. Time series observations of (**a**) rainfall, (**b**) water storage and estimated flux (Equation 1) in the vadose zone, and (**c**) change in groundwater hydraulic head and runoff in Elder Creek during the 2017 water year (from October 2016 to October 2017). The duration of the atmospheric river is bounded by the vertical dashed lines across all panels.
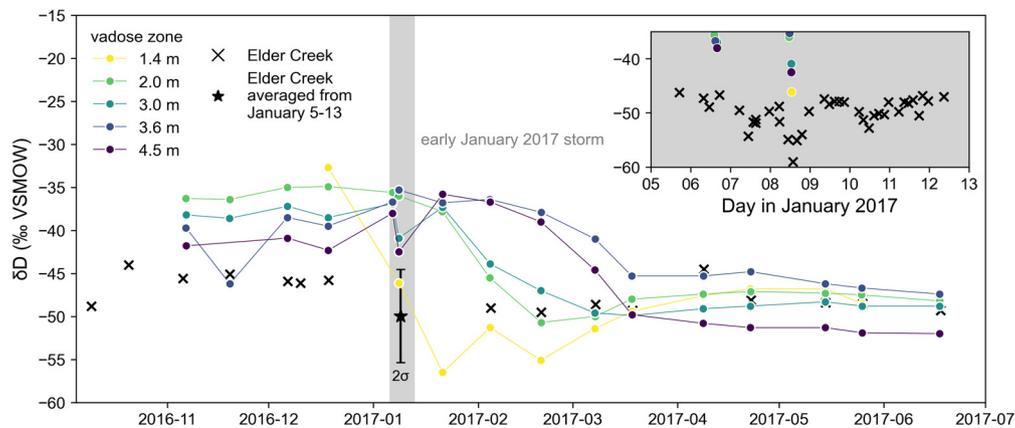
Fig. 3. A time series of the δD signal in Elder Creek and the shallow vadose zone waters at the location of the VMS. The shaded area marks the period of the atmospheric river. The data from high-resolution sampling of Elder Creek during this time (individually shown on the inset plot) are averaged in order to be more comparable to the sparse, long-term data set.

through soils do not contribute to runoff (Rempe and Dietrich, 2018; Salve et al., 2012). During the January 2017 storm event, neither was observed along the hillslope. Therefore, flow through the vadose zone to the water table kept pace with the intensity of rainfall.

3.2. Stable isotopes of water

The atmospheric river that produced this storm delivered a substantial volume of isotopically depleted water (δD $= -86\permil$; Fig. S3). This depleted signature was detected within the hillslope using the unique instrumentation of the VMS (Fig. 3). The propagation of the depleted δD signature in the weathered bedrock vadose zone mimics a breakthrough curve. At 1.4 m depth, the signal arrived 8 days after the end of the storm event while the arrival at 4.5 m took 64 days. Notably, this transmitted storm signal appears attenuated at depth, measuring $-50\permil$ at 4.5 m versus $-55\permil$ at 1.4 m.

In Elder Creek, high-frequency stream sampling revealed larger variability in δD during the timescale of the storm relative to the vadose zone (inset in Fig. 3). As discharge peaked in response to the storm, stream water showed isotopic depletion to as much as $-59\permil$, suggesting that water from the storm event directly entered the stream as precipitation. However, at the time that streamwater was showing depletion, the isotopic signature of the storm had only penetrated to ≤ 1.4 m within the VMS along the Rivendell hillslope. This observation implies that the storm water only gradually traversed the subsurface, which will be important to the interpretation of subsurface reactivity.

3.3. Strontium isotopes

Radiogenic ^{87}Sr/^{86}Sr values of groundwater sampled across the hillslope and Elder Creek are consistent within analytical uncertainty and average 0.70977 ± 3 (Fig. S4a). These fluids are all slightly lower than the fresh bedrock (^{87}Sr/^{86}Sr $= 0.70984 \pm 3$). Therefore, there is negligible variability in groundwater ^{87}Sr/^{86}Sr
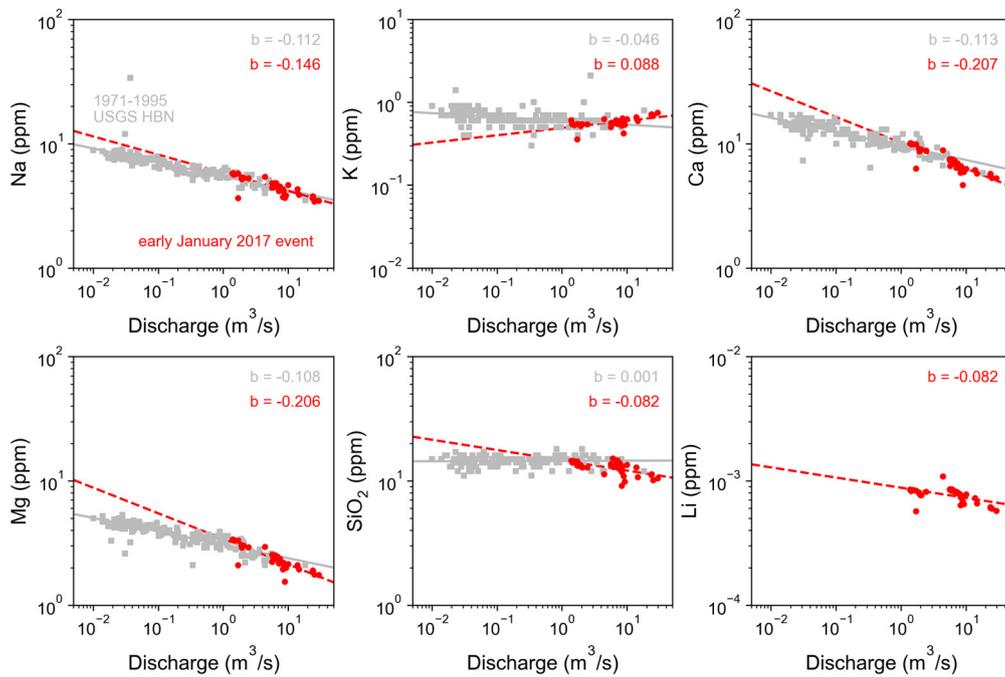
Fig. 4. Concentration-discharge profiles of Elder Creek rock-derived solutes. The points represent observations from this study (red circles) and the USGS Hydrologic Benchmark Network program (gray squares; Clark et al., 2000) with corresponding lines that show a fitted power law in the form of $C = aQ^b$ (Godsey et al., 2009; Musolff et al., 2015), where b is the logC-logQ slope.

across the hillslope and into the stream, as well as between samples collected prior to and during the storm. Furthermore, the differences between fluid and solid-phase samples reported here are small compared to variations observed in other sites of similar lithology (e.g., Chapman et al., 2012; Meek et al., 2016).

3.4. C-Q behavior

As previously reported (Godsey et al., 2009; Maher, 2011), chemostatic conditions are reflected in the long-term C-Q patterns at Elder Creek (Fig. 4). Despite the intensity of this storm, the new data appear to largely extrapolate long-term export behavior, although some solutes slightly trend towards dilution (b = -1). An exception to this consistency is noted for potassium, where the b-exponent during the storm shifts to a positive value, implying mobilization (b = 1). This deviation may be a result of the strong biological influences exerted on potassium (e.g., plant uptake; Knapp et al., 2020; Rose et al., 2018). One study even argues for positive storm C-Q relationships including potassium due to exposure of fresh reactive mineral surface associated with physical crushing of rock in the stream channel (Morin et al., 2014), although we see no evidence of this for other solutes. While there are no historical data to reference, the C-Q behavior of Li appears to generally follow that of the major geogenic solutes, particularly silica.

Clearly, a wealth of information is contained within these storm data and in relation to the long-term records for these solutes. Here, we utilize these data specifically to analyze the extent to which high-intensity events are extrapolations of long-term behavior, and hence should ultimately reflect an expansion of the same underlying water-rock-life weathering reactions to more extreme conditions.

3.5. Lithium isotopes

Solute concentrations and δ^7Li values are corrected for atmospheric inputs (Supplementary Text S2) in order to isolate subsurface contributions (further discussed in subsection 4.1 and sub-

section 4.3). These corrections indicate that the contribution to dissolved Li by atmospheric inputs is <2%. Correspondingly, the maximum fraction of Li derived from rainwater would only adjust the measured values by +0.52‰ to +0.58‰ in the range of δ^7Li observed in Elder Creek (+26‰ to +29‰) and is within the analytical uncertainty of ±0.76‰. Thus, we consider this contribution as negligible and do not apply a correction to the δ^7Li values. In addition, we normalize rain-corrected Li concentrations (hereinafter referred to as Li*) to Na* values to eliminate the effects of dilution in Li concentrations (Supplementary Text S2).

Li dynamics over the course of the storm event reveal a general increase in Li*/Na* and a decrease in δ^7Li (Fig. 5). The δ^7Li signature decreased from a maximum of +28.9 ± 0.1‰ to as low as +26.4 ± 0.4‰ at the height of the storm. In contrast, the initial Li*/Na* ratio increased by 0.24 μM/mM to reach a maximum of 0.82 μM/mM. However, the maximum Li*/Na* value was observed on the falling limb of the hydrograph, whereas the minimum δ^7Li was observed at peak discharge. Critically, both trends (decreasing δ^7Li and increasing Li*/Na*) reflect an approach to bedrock values (δ^7Li = −0.57‰ and Li*/Na* = 10.5 μM/mM; Golla et al., 2021). We reiterate that these values are corrected for atmospheric inputs, and that the effects of dilution on Li* concentrations are removed through normalization to Na*.

4. Discussion

4.1. Impact of the storm on subsurface water storage and flow

Consistent with observations of hydrological dynamics at the site (Rempe and Dietrich, 2018; Salve et al., 2012), precipitation delivered during this intense storm was routed through the bedrock vadose zone. This infiltration is evidenced by both the increases in vadose zone water flux and water table elevation concurrent with the storm (Fig. 2) and the breakthrough of a depleted δD signature in the vadose zone (Fig. 3). The subsurface transmission of such an intense storm event highlights the important role of rock moisture during the wet season in the routing of precipitation to drainage networks (Rempe and Dietrich, 2018). Such
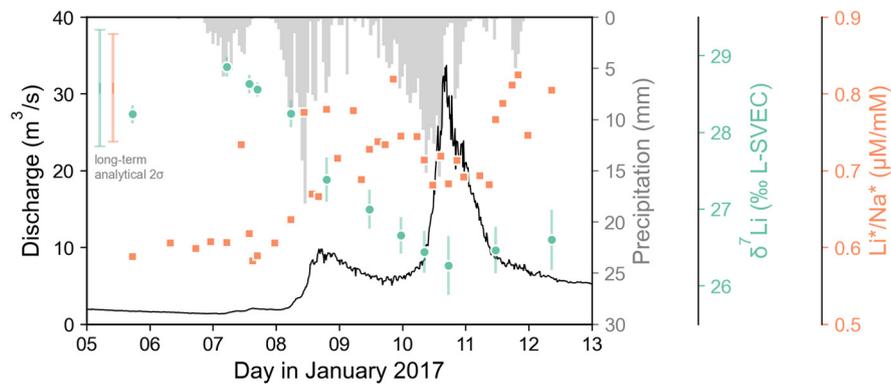
Fig. 5. Time series of lithium isotope ratios (green circles) and Li*/Na* ratios (Equation S1, orange squares) overlain on a hydrograph of Elder Creek and corresponding hyetograph during the atmospheric river. The sample-specific error bars denote the 95% confidence interval calculated from Equation 4. In addition, long-term analytical uncertainties of elemental concentrations (estimated as ±10% by propagating ±5% associated to each element during atmospheric corrections and normalization) and δ^7Li (±0.76‰; as explained in subsection 2.3) are also shown in the upper left corner.

behavior is distinct from systems in which high-flow periods produce a large contribution of "young" water (i.e. shallow soil water or water that may not have even reached the subsurface at all) to the stream at the peak of the storm (e.g., Benettin et al., 2020; McGuire and McDonnell, 2006).

Rock moisture and groundwater contributions to streamflow during this intense storm event increased on the timescale of the storm itself. This is consistent with recent laboratory (Guérin et al., 2014) and field observations (Guérin et al., 2019) indicating a characteristic scaling relationship between rapid responses in runoff and groundwater flow rates during storms in small catchments (Fig. S5). Yet, the water isotope data indicate that groundwater was not composed of precipitation from this storm event. Rather, the progressive attenuation of the storm δD signal in the vadose zone with depth indicates mixing of the event water with vadose zone water storage, effectively displacing pre-existing rock moisture into the saturated zone (Fig. 3). While preferential flowpaths in some fractured bedrock dominated hillslopes may contribute significant event water to recharge or streamflow (Nimmo et al., 2002; Sidle et al., 2000), here, we observe that the timescale at which fluid is transported through the hillslope lags significantly behind the instantaneous response of subsurface flow rates and streamflow to the event pulse (i.e., celerity; Fig. 2) as evidenced by the transmission of the storm δD signal over the course of a few months in the vadose zone (Fig. 3). This observed difference is consistent with the 'old water paradox' (Kirchner, 2003) and is an important consideration for hillslope runoff generation with respect to the resulting distribution of fluid travel times (McDonnell and Beven, 2014) and thus the extent of fluid-rock interaction reflected by streamflow. Given that fluid was displaced from the interior of the actively weathering hillslope by infiltration of the storm, the interior structure and reactivity of the hillslope must be considered in interpretation of stream weathering signatures.

While all water travels through the vadose zone to groundwater, the variable thickness of the vadose zone leads to different length scales and thus timescales of fluid transport through the system as a function of hillslope position. Vadose zone thickness is observed to correspond with the thickness of weathered bedrock, which tends to increase upslope (e.g., Rempe and Dietrich, 2018). This relationship means that locations higher up the hillslope show larger dynamic vadose zone water storage and thus require a larger volume of fluid to be refilled seasonally in order to trigger groundwater recharge (Rempe and Dietrich, 2018; Schmidt and Rempe, 2020). As a result, groundwater levels where vadose zone water storage is smaller (i.e., downslope) respond relatively faster to rainfall (Salve et al., 2012).

Altogether, our results imply a continuity in the hydrogeochemical system rather than a bypassing of the near-surface, where fluid stored downslope should represent a significant contribution to the stream during the storm. Given our interpretation of hydrological dynamics during the event, the fluid-rock reactivity from soil through vadose zone to groundwater remains relevant to the generation of geochemical signatures observed in the stream during this high intensity storm.

4.2. Geochemical evidence of continuity in reaction pathways

In subsection 4.1, we argue that hydrologic flowpaths from infiltration to vadose zone to groundwater to stream are maintained throughout an intense storm event. Now, we verify continuation in the geochemical reaction network during this storm event relative to ambient periods. First, the spatially and temporally homogeneous distribution of groundwater and Elder Creek ^{87}Sr/^{86}Sr (Fig. S4a) indicates there is no detectable shift in the distribution of minerals undergoing dissolution and thus the flow path accessed by groundwater. This is based on the expectation that the dissolved ^{87}Sr/^{86}Sr signature is inherited from the solid material(s) releasing solutes to water (e.g., Bullen et al., 1997; Négrel et al., 2018). Although sparser, the groundwater δ^7Li data appear to similarly suggest a preservation of subsurface flow paths and associated secondary phase formation, maintaining the relative magnitude and pattern of increase in values downslope before and during the event (Fig. S4b). While there is some variation in δ^7Li within individual wells between the two sampling dates, we emphasize that there is no systematic trend, and we lack a sufficient record of temporal variation in the groundwater δ^7Li to draw further inference from individual well variability. Furthermore, the wells are fully screened and therefore represent a mixture of depths below the water table, leading to some homogenization in these isotope ratios. Hence, we only use these observations to note that there is no systematic difference in the spatial pattern of this record across the duration of the storm. These inferences of invariant mineral dissolution and precipitation support the continuity of subsurface (bio)geochemical reactions that contribute to Elder Creek even during an intense storm event.

Next, we consider whether a variable contribution from a distinct shallow-soil end member could offer a viable explanation of the stream δ^7Li observations. This would follow the reasoning that the storm event promoted greater hydrological connectivity, and as a consequence, shallow water stores may have become preferentially mobilized, essentially bypassing the deeper subsurface. If true, we would anticipate δ^7Li signatures that are isotopically light, as is typical of shallow soil waters (Lemarchand et al., 2010), and

Table 2

Parameters for simple mixing (Fig. S6) and the reaction (Fig. 6) models. The variables denoting the Li composition of fluids equilibrated with soil ($\frac{Li}{Na}_{soil}$, $\delta^7 Li_{soil}$) and bedrock ($\frac{Li}{Na}_{bedrock}$, $\delta^7 Li_{bedrock}$) are used in the mixing model equations in Supplementary Text S3. In the reaction models, $\frac{Li}{Na}_o$ and $\delta^7 Li_o$ refer to the initial Li composition from which the fluid evolves, $\delta^7 Li_{diss}$ is the dissolution flux (Equation (6); Lemarchand et al., 2010), and $\alpha_{sec-diss}$ is the Li isotope fractionation factor associated to precipitation of secondary minerals. The tabulated $\frac{Li}{Na}_{soil}$ and $\delta^7 Li_{soil}$ values are the mean and associated 2σ of shallow (0-30 cm) soil waters in Lemarchand et al. (2010, their Table 2).

Fixed parameter(s)	Value(s)	Source
$\frac{Li}{Na}_{soil}$	6.9 ±5.6 μM/mM	Lemarchand et al. (2010)
$\delta^7 Li_{soil}$	−10.9 ±8.2‰	Lemarchand et al. (2010)
$\frac{Li}{Na}_{bedrock}$, $\frac{Li}{Na}_o$	10.6 μM/mM	Golla et al. (2021)
$\delta^7 Li_{bedrock}$, $\delta^7 Li_o$, $\delta^7 Li_{diss}$	−0.57‰	Golla et al. (2021)
$\alpha_{sec-diss}$	0.9898 (Rayleigh), 0.975 (Lemarchand)	Fitted

could potentially explain the decrease in δ^7Li signatures during the storm.

A theoretical binary mixture between water equilibrated with shallow soil and water equilibrated with bedrock is produced by weighing each end member fraction by its respective Li/Na ratio (Supplementary Text S3; Fig. S6). All parameter values are given in Table 2. While this mixing approach is capable of achieving the range of low Li*/Na* values seen in Elder Creek during the storm (0.6-0.8 μM/mM) using the soil water end member, it is unable to capture the high δ^7Li values (+26‰ to +29‰). Furthermore, although the δ^7Li of the bedrock-equilibrated water can be adjusted to represent the isotopically heavier groundwater previously observed at the site (+23‰ to +25‰), the lowest Li*/Na* ratios that correspond to these samples are still greater than 2 μM/mM (Golla et al., 2021). Overall, these results indicate that mixing between soil- and bedrock-equilibrated fluid end members, and thus transport processes alone, cannot explain the Li trends during the storm. Therefore, isotopically fractionating reactions that occur along subsurface fluid flowpaths must contribute to the δ^7Li signature of Elder Creek during the storm.

4.3. Toward coupled transport and reactivity

Despite the magnitude of the storm event, very little change is observed in the major solute C-Q behavior (Fig. 4), further suggesting that the (bio)geochemical reactions that produce observed solute signatures in Elder Creek during hydrological quiescence are still in effect. This inference is supported by our combination of physical hydrologic observations, water isotope tracing, groundwater ^{87}Sr/^{86}Sr ratios, and mixing model analysis, all of which suggest that the same basic routing of water through the subsurface and (bio)geochemical reactivity therein continue to apply during this storm.

If fractionating geochemical reactions are producing our observed δ^7Li in Elder Creek, the relationship should be describable with basic models relating isotopic enrichment to reaction progress. Rayleigh models are widely applied for this purpose, and have been previously utilized in application to δ^7Li and other isotope systems in weathering environments (e.g., Dellinger et al., 2015; Fernandez et al., 2022; Georg et al., 2007). In the following functional form

$$\delta^7 Li = \delta^7 Li_o + 1000(\alpha_{sec-diss} - 1) ln(f^{Li}_{diss}),\qquad(5)$$

$\delta^7 Li_o$ is the initial isotope composition of the fluid, $\alpha_{sec-diss}$ is the isotopic fractionation factor between the actively forming secondary minerals and the fluid, and f^{Li}_{diss} is the fraction of Li left in solution. The value of f^{Li}_{diss} is calculated by normalizing the Li*/Na* ratio of the fluid to the Li/Na ratio of fresh bedrock (e.g., Dellinger et al., 2015).

From a starting point of $f^{Li}_{diss} = 1.0$ (i.e., congruent dissolution), the Rayleigh calculation can be used for any given value

of $f^{Li}_{diss} < 1.0$ and an associated fractionation factor $\alpha_{sec-diss}$. For our parameterization (Table 2), we recover the observed trend in Li*/Na* and δ^7Li in the stream (Fig. 6a) with an $\alpha_{sec-diss} = 0.9898$. The sensitivity of this result to the choice of $\frac{Li}{Na}_{bedrock}$ is explored in Supplementary Text S4. This $\alpha_{sec-diss}$ value is lower, or more "muted", relative to the typical range of values isolated in laboratory studies of δ^7Li fractionation during formation of common clays such as illite and smectite (e.g., Hindshaw et al., 2019; Vigier et al., 2008; Williams and Hervig, 2005). This apparent dampening of the isotopic fractionation factor could result from the compounding effects of multiple contemporaneous solubilization and precipitation reactions and/or as a result of averaging over a distribution of flow paths (Druhan and Maher, 2017).

For our purpose, the key observation taken from the Rayleigh model (Fig. 6a) is that δ^7Li values measured during the event show less reaction progress along the Rayleigh trend, indicating less geochemical evolution from a starting bedrock-equilibrated fluid value. In contrast, lower discharge values before the rising limb of the event show more enriched δ^7Li and lower f^{Li}_{diss}, suggesting more reaction progress. In total, this relationship suggests that during the storm subsurface fluid contributing to Elder Creek was less reacted, as would be associated with a faster mean subsurface fluid travel times.

Certainly there are limitations to the applicability of a simple Rayleigh model, including the assumption that Li is only lost from solution from a starting point that is bedrock-equilibrated, rather than contemporaneous solubilization of primary minerals (δ^7Li ≈ 0‰) and formation of new secondary phases. To build upon this basis, we next utilize a batch-reactor model that considers the simultaneous effects of mineral dissolution and precipitation (Fig. 6b; Lemarchand et al., 2010)

$$\begin{aligned}
\delta^7 Li = &\ \delta^7 Li_o - \lambda 1000(\alpha_{sec\text{-}diss} - 1) \\
& + (\delta^7 Li_o + 1000(\alpha_{sec\text{-}diss} - 1) \\
& - \delta^7 Li_{diss}) \times \left(\frac{(Li/Na)_o}{(Li/Na)} \right)^{\frac{1}{1-\lambda}},
\end{aligned}\qquad(6)$$

where $(Li/Na)_o$ and $\delta^7 Li_o$ are the initial compositions of the fluid, $\delta^7 Li_{diss}$ is the dissolution flux, and λ is the ratio between the mineral precipitation and dissolution fluxes. Once again, the model simulates the reaction pathway from a bedrock-equilibrated fluid. In this framework, the Lemarchand et al. (2010) model is able to match the range of values observed in Elder Creek during the storm for a $\alpha_{sec-diss} = 0.975$ (Table 2). This fractionation factor is more comparable to the range of intrinsic or laboratory-derived $\alpha_{sec-diss}$ of clays ($\alpha_{smectite-diss} = 0.9834$ and $\alpha_{illite-diss} = 0.976$; Hindshaw et al., 2019; Williams and Hervig, 2005) that are predominantly forming at depth at this site (Golla et al., 2021; Gu et al., 2020).
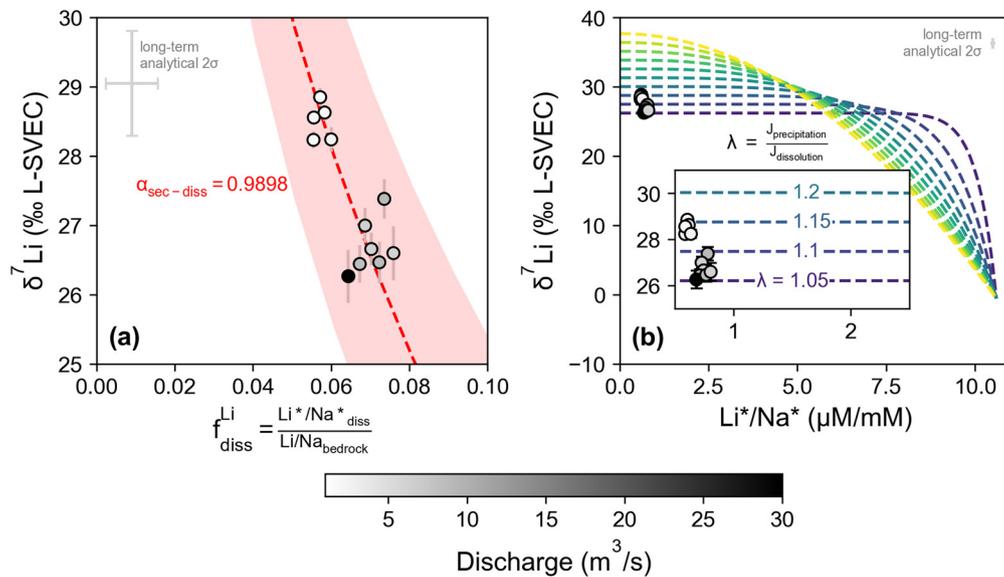
Fig. 6. Observations (circles) and results of models for Rayleigh isotope fractionation (**a**), and mineral precipitation and dissolution in a well-mixed system (Lemarchand et al., 2010) (**b**). The light-red shaded envelope in panel (**a**) is the 95% confidence interval of the fitted Rayleigh model curve. The sample-specific error bars denote the 95% confidence interval calculated from Equation 4 while the long-term analytical uncertainties are provided in the upper corner as in Fig. 5.

In this framework, the decrease in δ^7Li observed during the storm is attributed to a decrease in the extent of secondary mineral precipitation (or a decreasing λ coefficient). As in the Rayleigh framework, this result also suggests that the Li composition of Elder Creek during the storm was less geochemically evolved (from a starting point of bedrock-equilibrated fluid) than that before the rising limb of the hydrograph. In total, these simple modeling exercises demonstrate that isotopically fractionating geochemical reactions remain relevant to the interpretation of stream Li even during an intense storm. Furthermore, they suggest contemporaneous solubilization and precipitation of multiple mineral phases, which requires a multi-component numerical reactive transport simulation to be fully encapsulated. From this basis, we proceed with application of our previously validated 1-D reactive transport model framework for δ^7Li signatures of fluids draining through the near-surface of this system (Golla et al., 2021).

4.4. Application of a coupled reactive transport modeling framework to the stream δ^7Li signatures of a large storm

Our previously established 1-D reactive transport model framework is designed to trace the evolution of Li and its stable isotopes through the Rivendell hillslope via an ensemble of silicate weathering reactions (primary mineral dissolution, clay solubilization, and clay formation; Supplementary Text S5; Golla et al., 2021). This framework is based on a vadose zone reactive transport model that simulates the interaction between infiltrating meteoric fluids and the modern-day regolith underlying the Rivendell hillslope. The model domain is partitioned into multiple distinct sub-domains in order to reflect the compositional gradient of the weathering profile (Wang, 2020) as observed in the solid-phase geochemistry and mineralogy (Gu et al., 2020). As a result, the model solid-phase profile varies chemically (Li/Na = 4.5-10 mM/M) and isotopically (δ^7Li = -12 to -0.57‰) with depth. Simulation of lateral drainage below the water table is initiated using the conditions taken from the base of the 1-D vadose zone model. The fluid in the saturated zone is allowed to continue geochemically evolving through time from this initial condition. Given the sensitivity of Li isotopes to the formation of secondary minerals (e.g., Huh et al., 2001; Pistiner and Henderson, 2003; Rudnick et al., 2004), we used δ^7Li signatures of fluids from the VMS to further constrain

the multiple-mineral weathering reaction network of the model, which was only previously calibrated by major solute observations (Wang, 2020). Further details about the parameterization and development of the model can be found in Supplementary Text S5 and Golla et al. (2021).

An important outcome of this previous modeling framework is the distinction between the vadose zone, which acts as net source of Li to the dissolved load, and the saturated aquifer, which acts as a sink of Li from the fluid. The Golla et al. (2021) model indicates that Li concentrations increase across the vadose zone by 0.87 μM and attendant Li/Na increase by 9 μM/mM. In contrast, 0.45 μM of Li is lost from groundwater as it transits from the upper hillslope to the toe, associated with a decrease in Li/Na of 7 μM/mM. Throughout the system, δ^7Li enriches as a result of the formation of multiple secondary mineral phases. This compartmentalization of Li source (vadose zone) and sink (saturated zone) across the hillslope is highly relevant to our analysis of stream chemistry, which serves as the terminus of these reactive flow paths.

As a new expansion of this previous approach, we run additional simulations to produce a solution space that encapsulates two factors. First, we simulate a range of vadose zone depths for further geochemical evolution in the saturated zone (Fig. 7). This may be translated into distinct locations along the hillslope, as the vadose zone becomes progressively thicker from toe to ridge. Each of these flow paths offers a representation of the typical extent of subsurface contribution to the dissolved Li load of Elder Creek as a function of distance upslope. Analyzing multiple flow paths in this way allows us to simulate the effects of the storm on subsurface drainage that emerge as a function of internal weathered bedrock thickness and vadose zone water storage capacity (subsection 4.1). In general, the saturated zone geochemical evolution initiates from higher Li/Na ratios when sourced from a thicker vadose zone (i.e., further upslope). Secondly, from any given initial condition in the saturated zone model, the simulated trajectory of increasing δ^7Li and decreasing Li/Na evolves with time due to fluid-rock reactivity, such that the value achieved at the terminus of the hillslope (i.e., the stream) is a function of the fluid flow rate. Analyzing flow rates in this way allows us to study the effects of changing subsurface fluid velocities in response to the storm event (subsection 3.1; Fig. 2).
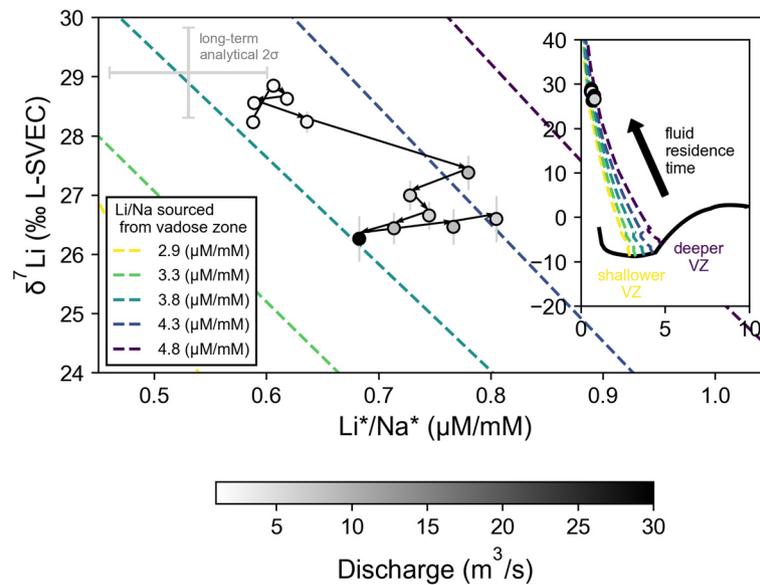
Fig. 7. Observations (circles) are connected by arrows that indicate the progression of the storm event. The dashed lines represent the various flow paths simulated by allowing the saturated zone model in Golla et al. (2021) to geochemically evolve from a range of depths between the soil surface and the water table (denoted as Li/Na sourced from vadose zone). Inset depicts the original 1-D vadose zone reactive transport model (Golla et al., 2021) and the trajectories of these saturated-zone simulations from various starting points (depths) along the vadose zone solution space. The sample-specific error bars denote the 95% confidence interval calculated from Equation 4 while the long-term analytical uncertainties are provided in the upper corner as in Fig. 5.

The range of δ^7Li and Li/Na taken from the base of our vadose zone model and used as initial conditions in our saturated zone model fall between δ^7Li = −8.7 to −6.1‰ and Li/Na = 2.9-4.8 µM/mM (Fig. 7). These compositions correspond to a vadose zone thickness ranging between 2 m (lower Li/Na) and 4 m (higher Li/Na), which is generally consistent with the thickness of weathered bedrock at the base of the hillslope (4 m; Rempe and Dietrich, 2018). This result suggests that a significant proportion of the Li that appears in the stream must be sourced from downslope, which is consistent with a greater response in the groundwater table downslope over the timescale of storm events (subsection 4.1; Rempe and Dietrich, 2018; Salve et al., 2012). A key point in this analysis is that all flow paths within the hillslope are routed to the stream and, hence, contribute to stream chemistry, meaning fluids that infiltrated further upslope are still present in streamflow during the storm. Some of the solubilized Li in these longer flow paths is lost to secondary mineral precipitation, as evidenced by continued enrichment in δ^7Li (Golla et al., 2021). What remains in solution mixes with Li sourced from further downslope and appears in the stream as a spatially integrated signal reflecting both flux weighting of fluid flow paths and the distribution of fluid-rock reactivity across the interior of the hillslope (Fig. 8).

To draw further inference from this model-data comparison, we partition observations taken during the storm from those at lower discharge rates prior to the rising limb of the storm (Fig. 7). During the storm, both δ^7Li and Li*/Na* measurements are consistent with a combination of (1) deeper vadose zone depths and (2) shorter fluid residence times. This inference is supported by our model results. First, shorter fluid residence times in the groundwater produce lower δ^7Li (inset in Fig. 7) due to less secondary mineral formation. However, the data observed during the storm show higher Li*/Na* values (relative to those prior to the storm) than what can be produced in a single simulation simply by decreasing fluid residence time. Hence, an overall increase in subsurface flow rates is necessary, but cannot exclusively explain the shift in Li composition from low- to high-discharge conditions. In addition, the model requires a higher initial δ^7Li and Li/Na starting point, corresponding to a deeper vadose zone, in order to produce the shift in the stream data at higher flow rates during the storm.

As a consequence, the juxtaposition of our model with the observed δ^7Li and Li*/Na* signatures of the storm event suggests a discernable shift toward a greater contribution of Li to the stream sourced from further upslope, where the vadose zone is thicker. As demonstrated by our process-based model, this change in provenance is coupled to an increase in subsurface flow rates. As the hillslope fills during the storm, groundwater flows faster towards the stream, and the rising water table accesses and mobilizes Li from the base of the vadose zone, leading to the delivery of overall less-reacted Li (lower δ^7Li, higher Li/Na) from a larger source area (Fig. 8). Importantly, the chemical signatures recorded in the stream are a result of water-rock interactions that precede and are generated over timescales longer than that of the rain event (Golla et al., 2021). The perturbation imposed by the storm is merely shifting the relative contributions from the source (vadose zone) and sink (saturated zone) areas of Li within the hillslope. When treated in a reactive transport framework capable of describing multiple contemporaneous mineral dissolution and precipitation reactions, lithium isotopes recorded across the storm hydrograph offer the sensitivity necessary to disentangle the origin of rock-derived solute exports that ultimately produce C-Q relationships.

5. Conclusion

This study merges a wide variety of data and models to arrive at a coherent analysis of the export of rock-derived solutes by fluids draining through an actively weathering, upland hillslope during an intense storm and of the emergence of stream geochemical signatures across the storm hydrograph. An atmospheric river delivered an intense period of infiltration that combined with the shallow layers of a large volume of pre-existing rock moisture stored in the bedrock vadose zone above the water table. The displacement of this fluid caused the water table to rise and groundwater flow rates to increase, yet the underlying water-rock reactions producing rock-derived solutes within the interior of the hillslope remained consistent. Through a series of model exercises, we show that combined mineral dissolution and precipitation reactions are necessary to explain the δ^7Li data, ultimately supporting application of an isotope-enabled reactive transport model previ-
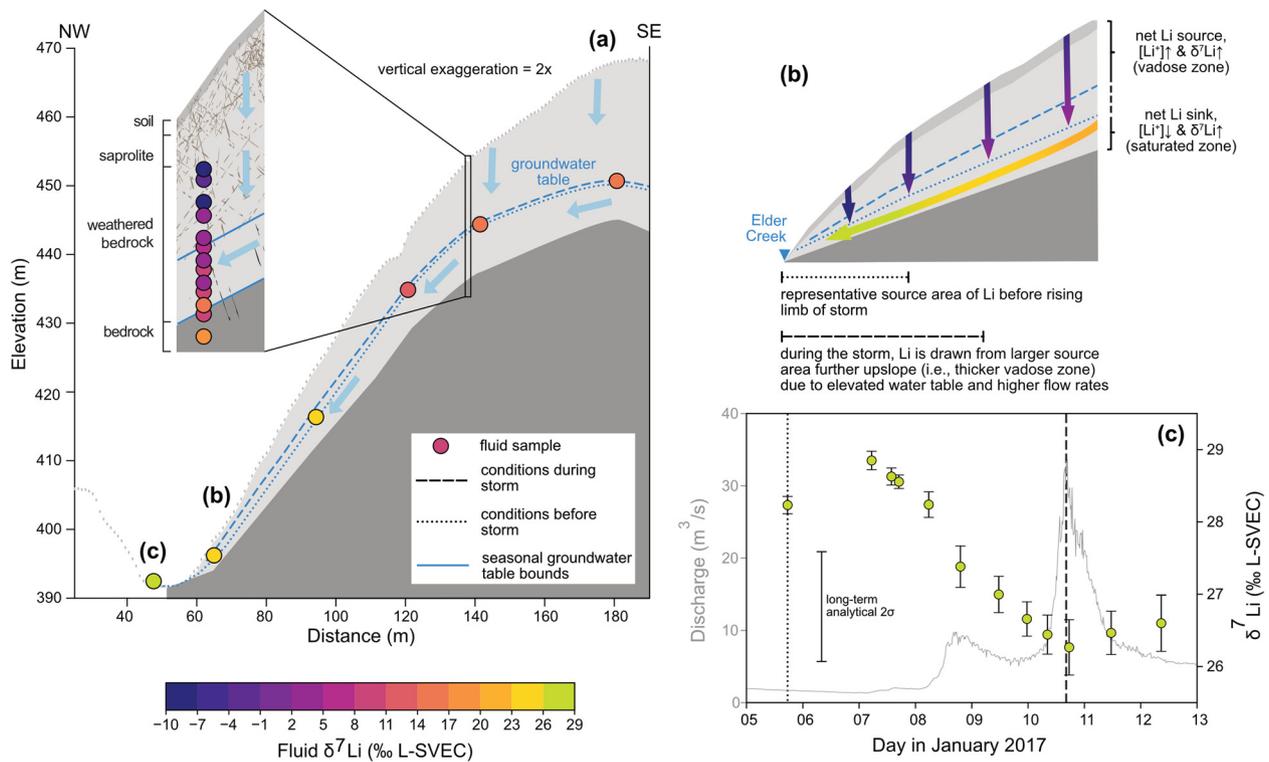
Fig. 8. A schematic of fluid δ^7Li evolution within the hillslope (**a**) shown in cross-section. The hillslope profile is modified after Rempe and Dietrich (2018) with the vertical axis exaggerated by 2x to highlight the change in groundwater table elevation during the storm. The location of samples taken from the Vadose Zone Monitoring System (VMS) and wells are illustrated with corresponding δ^7Li (color-graded circles) as reported in (Golla et al., 2021). The inset within (**a**) corresponds to the relative location of the VMS. Light blue arrows indicate direction of fluid flow within the hillslope. A smaller schematic (**b**; not to scale with respect to the cross section in **a**) illustrates the increased contribution of Li to the stream from further upslope where the vadose zone is thicker during the storm following Fig. 7. This is mimicked by the two dashed vertical lines in the storm hydrograph (**c**) and corresponding δ^7Li values in the stream as in Fig. 5.

ously developed for this site based on long-term solute sampling and δ^7Li collected under low-discharge conditions.

The combination of our model results and physical observations demonstrates a clear sensitivity of Li signatures to changes in subsurface flow as the hillslope fills during a large storm event. These isotope ratios are sensitive to the thickness of the bedrock vadose zone through which fluid drains, which acts as source of Li to the fluid phase. This solubilized Li continues to geochemically evolve within the saturated groundwater, which acts as a net sink of Li from the fluid, as it transits the hillslope (Fig. 8). Ultimately, the Li isotope composition of Elder Creek recorded during this large storm provides a new lens within the characteristically chemostatic solute signatures of Elder Creek, revealing connectivity between subsurface structure and function and the geochemistry of streamwater under transient hydrological conditions. This conceptual model (Fig. 8) does not support shallow soil water or overland flow as predominant contributors to stream δ^7Li signatures during storm events. Rather, these findings open the opportunity to leverage models for the reactive transport behavior occurring within hillslopes (Golla et al., 2021). This study motivates consideration of how such balances should differ among solutes based on the distribution of element-specific source and sink areas within a given system.

CRediT authorship contribution statement

Jon K. Golla: Conceptualization, Funding acquisition, Investigation, Methodology, Software, Writing – original draft, Writing – review & editing. **Julien Bouchez:** Conceptualization, Funding acquisition, Methodology, Resources, Validation, Writing – review & editing. **Marie L. Kuessner:** Funding acquisition, Methodology, Validation. **Daniella M. Rempe:** Conceptualization, Funding acquisition,

Methodology, Resources, Writing – review & editing. **Jennifer L. Druhan:** Conceptualization, Funding acquisition, Methodology, Resources, Software, Writing – original draft, Writing – review & editing.

Declaration of competing interest

The authors declare that they have no known competing financial interests or personal relationships that could have appeared to influence the work reported in this paper.

Data availability

Hydrological monitoring data are available on Dendra (https://dendra.science/) and the U.S. Geological Survey National Water Information System (https://waterdata.usgs.gov/nwis). All other materials can be accessed on CUAHSI HydroShare: Golla, J., J. Bouchez, M. Kuessner, D. M. Rempe, J. Druhan (2022). Accompanying data to Golla et al. (2022, EPSL) "Subsurface weathering signatures in stream chemistry during an intense storm", HydroShare, https://doi.org/10.4211/hs.d6e258cd5cb74bf18a4ef90177b4cd1d.

Acknowledgements

isotope analyses and Gunnar Reith and Will Speiser for help with sample collection. This research was partially funded by the People Programme (Marie Curie Actions) of the European Union Seventh Framework Programme FP7/2007-2013/ under REA agreement [608069] (ITN "IsoNose"), the IPGP multidisciplinary program PARI, and the Region île-de-France SESAME Grant No. 12015908. J.K.G. was supported by the NSF Graduate Research Fellowship Program. M.L.K. was supported by a joint OZCAR-CZEN fellowship. J.K.G., J.B., D.M.R., and J.L.D. acknowledge funding support from NSF-EAR-2047318. The Eel River Critical Zone Observatory was supported by NSF-EAR-1331940.

Appendix A. Supplementary material

Supplementary material related to this article can be found online at https://doi.org/10.1016/j.epsl.2022.117773.

References

Ameli, A.A., Beven, K., Erlandsson, M., Creed, I.F., McDonnell, J.J., Bishop, K., 2017. Primary weathering rates, water transit times, and concentration-discharge relations: a theoretical analysis for the critical zone. Water Resour. Res. 53, 942–960. https://doi.org/10.1002/2016WR019448. _eprint: https://onlinelibrary.wiley.com/doi/pdf/10.1002/2016WR019448.

Anderson, S.P., Dietrich, W.E., Torres, R., Montgomery, D.R., Loague, K., 1997. Concentration-discharge relationships in runoff from a steep, unchanneled catchment. Water Resour. Res. 33, 211–225. https://doi.org/10.1029/96WR02715. _eprint: https://onlinelibrary.wiley.com/doi/pdf/10.1029/96WR02715.

Arora, B., Burrus, M., Newcomer, M., Steefel, C.I., Carroll, R.W.H., Dwivedi, D., Dong, W., Williams, K.H., Hubbard, S.S., 2020. Differential C-Q analysis: a new approach to inferring lateral transport and hydrologic transients within multiple reaches of a mountainous headwater catchment. Front. Water 2. https://www.frontiersin.org/article/10.3389/frwa.2020.00024.

Baronas, J.J., Torres, M.A., Clark, K.E., West, A.J., 2017. Mixing as a driver of temporal variations in river hydrochemistry: 2. Major and trace element concentration dynamics in the Andes-Amazon transition. Water Resour. Res. 53, 3120–3145. https://doi.org/10.1002/2016WR019729. _eprint: https://onlinelibrary.wiley.com/doi/pdf/10.1002/2016WR019729.

Basu, N.B., Destouni, G., Jawitz, J.W., Thompson, S.E., Loukinova, N.V., Darracq, A., Zanardo, S., Yaeger, M., Sivapalan, M., Rinaldo, A., Rao, P.S.C., 2010. Nutrient loads exported from managed catchments reveal emergent biogeochemical stationarity. Geophys. Res. Lett. 37. https://doi.org/10.1029/2010GL045168. _eprint: https://onlinelibrary.wiley.com/doi/pdf/10.1029/2010GL045168.

Bazemore, D.E., Eshleman, K.N., Hollenbeck, K.J., 1994. The role of soil water in stormflow generation in a forested headwater catchment: synthesis of natural tracer and hydrometric evidence. J. Hydrol. 162, 47–75. https://doi.org/10.1016/0022-1694(94)90004-3. https://www.sciencedirect.com/science/article/pii/0022169494900043.

Benettin, P., Fovet, O., Li, L., 2020. Nitrate removal and young stream water fractions at the catchment scale. Hydrol. Process. 34, 2725–2738. https://doi.org/10.1002/hyp.13781. _eprint: https://onlinelibrary.wiley.com/doi/pdf/10.1002/hyp.13781.

Bieroza, M.Z., Heathwaite, A.L., 2015. Seasonal variation in phosphorus concentration–discharge hysteresis inferred from high-frequency in situ monitoring. J. Hydrol. 524, 333–347. https://doi.org/10.1016/j.jhydrol.2015.02.036. https://www.sciencedirect.com/science/article/pii/S0022169415001481.

Bullen, T., White, A., Blum, A., Harden, J., Schulz, M., 1997. Chemical weathering of a soil chronosequence on granitoid alluvium: II. Mineralogic and isotopic constraints on the behavior of strontium. Geochim. Cosmochim. Acta 61, 291–306. https://doi.org/10.1016/S0016-7037(96)00344-4. https://www.sciencedirect.com/science/article/pii/S0016703796003444.

Burton, K.W., Vigier, N., 2012. Lithium isotopes as tracers in marine and terrestrial environments. In: Baskaran, M. (Ed.), Handbook of Environmental Isotope Geochemistry: Vol. I. In: Advances in Isotope Geochemistry. Springer, Berlin, Heidelberg, pp. 41–59. https://doi.org/10.1007/978-3-642-10637-8_4.

Chanat, J.G., Rice, K.C., Hornberger, G.M., 2002. Consistency of patterns in concentration-discharge plots. Water Resour. Res. 38, 22. https://doi.org/10.1029/2001WR000971. _eprint: https://onlinelibrary.wiley.com/doi/pdf/10.1029/2001WR000971.

Chapman, E.C., Capo, R.C., Stewart, B.W., Kirby, C.S., Hammack, R.W., Schroeder, K.T., Edenborn, H.M., 2012. Geochemical and strontium isotope characterization of produced waters from Marcellus shale natural gas extraction. Environ. Sci. Technol. 46, 3545–3553. https://doi.org/10.1021/es204005g, publisher: American Chemical Society.

Clark, M.L., Eddy-Miller, C.A., Mast, M.A., 2000. Environmental Characteristics and Water Quality of Hydrologic Benchmark Network Stations in the West-Central United States, 1963-95. US Geological Survey, vol. 1173.

Dahan, O., Talby, R., Yechieli, Y., Adar, E., Lazarovitch, N., Enzel, Y., 2009. In situ monitoring of water percolation and solute transport using a vadose zone monitoring system. Vadose Zone J. 8, 916–925. https://doi.org/10.2136/vzj2008.0134. _eprint: https://acsess.onlinelibrary.wiley.com/doi/pdf/10.2136/vzj2008.0134.

Daly, C., Halbleib, M., Smith, J.I., Gibson, W.P., Doggett, M.K., Taylor, G.H., Curtis, J., Pasteris, P.P., 2008. Physiographically sensitive mapping of climatological temperature and precipitation across the conterminous United States. Int. J. Climatol. 28, 2031–2064. https://doi.org/10.1002/joc.1688. _eprint: https://onlinelibrary.wiley.com/doi/pdf/10.1002/joc.1688.

Daly, C., Smith, J.I., Olson, K.V., 2015. Mapping atmospheric moisture climatologies across the conterminous United States. PLoS ONE 10, e0141140. https://doi.org/10.1371/journal.pone.0141140. https://journals.plos.org/plosone/article?id=10.1371/journal.pone.0141140, publisher: Public Library of Science.

DeFlorio, M.J., Waliser, D.E., Guan, B., Lavers, D.A., Ralph, F.M., Vitart, F., 2018. Global assessment of atmospheric river prediction skill. J. Hydrometeorol. 19, 409–426. https://doi.org/10.1175/JHM-D-17-0135.1. https://journals.ametsoc.org/view/journals/hydr/19/2/jhm-d-17-0135_1.xml, publisher: American Meteorological Society.

Dellinger, M., Gaillardet, J., Bouchez, J., Calmels, D., Louvat, P., Dosseto, A., Gorge, C., Alanoca, L., Maurice, L., 2015. Riverine Li isotope fractionation in the Amazon River basin controlled by the weathering regimes. Geochim. Cosmochim. Acta 164, 71–93. https://doi.org/10.1016/j.gca.2015.04.042. http://www.sciencedirect.com/science/article/pii/S0016703715002483.

Diamond, J.S., Cohen, M.J., 2018. Complex patterns of catchment solute–discharge relationships for coastal plain rivers. Hydrol. Process. 32, 388–401. https://doi.org/10.1002/hyp.11424. _eprint: https://onlinelibrary.wiley.com/doi/pdf/10.1002/hyp.11424.

Druhan, J.L., Maher, K., 2017. The influence of mixing on stable isotope ratios in porous media: a revised Rayleigh model. Water Resour. Res. 53, 1101–1124. https://doi.org/10.1002/2016WR019666. _eprint: https://agupubs.onlinelibrary.wiley.com/doi/pdf/10.1002/2016WR019666.

Dunne, T., Black, R.D., 1970a. An experimental investigation of runoff production in permeable soils. Water Resour. Res. 6, 478–490. https://doi.org/10.1029/WR006i002p00478. _eprint: https://onlinelibrary.wiley.com/doi/pdf/10.1029/WR006i002p00478.

Dunne, T., Black, R.D., 1970b. Partial area contributions to storm runoff in a small new England watershed. Water Resour. Res. 6, 1296–1311. https://doi.org/10.1029/WR006i005p01296. _eprint: https://onlinelibrary.wiley.com/doi/pdf/10.1029/WR006i005p01296.

Evans, C., Davies, T.D., 1998. Causes of concentration/discharge hysteresis and its potential as a tool for analysis of episode hydrochemistry. Water Resour. Res. 34, 129–137. https://doi.org/10.1029/97WR01881. _eprint: https://doi.org/10.1029/97WR01881.

Fernandez, N.M., Bouchez, J., Derry, L.A., Chorover, J., Gaillardet, J., Giesbrecht, I., Fries, D., Druhan, J.L., 2022. Resiliency of silica export signatures when low order streams are subject to storm events. J. Geophys. Res., Biogeosci. 127, e2021JG006660. https://doi.org/10.1029/2021JG006660. _eprint: https://onlinelibrary.wiley.com/doi/pdf/10.1029/2021JG006660.

Flesch, G., Anderson Jr, A., Svec, H., 1973. A secondary isotopic standard for $^6Li/^7Li$ determinations. Int. J. Mass Spectrom. Ion Phys. 12, 265–272. Publisher: Elsevier.

Fries, D.M., James, R.H., Dessert, C., Bouchez, J., Beaumais, A., Pearce, C.R., 2019. The response of Li and Mg isotopes to rain events in a highly-weathered catchment. Chem. Geol. 519, 68–82. https://doi.org/10.1016/j.chemgeo.2019.04.023. https://www.sciencedirect.com/science/article/pii/S0009254119302062.

Frings, P.J., Oelze, M., Schubring, F., Frick, D.A., Blankenburg, F.V., 2021. Interpreting silicon isotopes in the critical zone. Am. J. Sci. 321, 1164–1203. https://doi.org/10.2475/08.2021.02. https://www.ajsonline.org/content/321/8/1164.

Fuller, T.K., Perg, L.A., Willenbring, J.K., Lepper, K., 2009. Field evidence for climate-driven changes in sediment supply leading to strath terrace formation. Geology 37, 467–470. https://doi.org/10.1130/G25487A.1. https://pubs.geoscienceworld.org/gsa/geology/article-abstract/37/5/467/29957/Field-evidence-for-climate-driven-changes-in, publisher: GeoScienceWorld.

Gaillardet, J., Lemarchand, D., 2018. Boron in the weathering environment. In: Marschall, H., Foster, G. (Eds.), Boron Isotopes: The Fifth Element. In: Advances in Isotope Geochemistry. Springer International Publishing, Cham, pp. 163–188. https://doi.org/10.1007/978-3-319-64666-4_7.

Gardner, C.B., Litt, G.F., Lyons, W.B., Ogden, F.L., 2017. Evidence for the activation of shallow preferential flow paths in a tropical Panama watershed using germanium and silicon. Water Resour. Res. 53, 8533–8553. https://doi.org/10.1002/2017WR020429. _eprint: https://onlinelibrary.wiley.com/doi/pdf/10.1002/2017WR020429.

Georg, R.B., Reynolds, B.C., West, A.J., Burton, K.W., Halliday, A.N., 2007. Silicon isotope variations accompanying basalt weathering in Iceland. Earth Planet. Sci. Lett. 261, 476–490. https://doi.org/10.1016/j.epsl.2007.07.004. https://www.sciencedirect.com/science/article/pii/S0012821X07004530.

Godsey, S.E., Kirchner, J.W., Clow, D.W., 2009. Concentration–discharge relationships reflect chemostatic characteristics of US catchments. Hydrol. Process. 23, 1844–1864. https://doi.org/10.1002/hyp.7315. _eprint: https://onlinelibrary.wiley.com/doi/pdf/10.1002/hyp.7315.

Golla, J.K., Kuessner, M.L., Henehan, M.J., Bouchez, J., Rempe, D.M., Druhan, J.L., 2021. The evolution of lithium isotope signatures in fluids draining ac-

tively weathering hillslopes. Earth Planet. Sci. Lett. 567, 116988. https://doi.org/10.1016/j.epsl.2021.116988. https://www.sciencedirect.com/science/article/pii/S0012821X21002478.

Gu, X., Rempe, D.M., Dietrich, W.E., West, A.J., Lin, T.C., Jin, L., Brantley, S.L., 2020. Chemical reactions, porosity, and microfracturing in shale during weathering: the effect of erosion rate. Geochim. Cosmochim. Acta 269, 63–100. https://doi.org/10.1016/j.gca.2019.09.044. http://www.sciencedirect.com/science/article/pii/S0016703719306386.

Guérin, A., Devauchelle, O., Lajeunesse, E., 2014. Response of a laboratory aquifer to rainfall. J. Fluid Mech. 759. https://doi.org/10.1017/jfm.2014.590. https://www.cambridge.org/core/journals/journal-of-fluid-mechanics/article/response-of-a-laboratory-aquifer-to-rainfall/900705285256BFBE309692971805B505, publisher: Cambridge University Press.

Guérin, A., Devauchelle, O., Robert, V., Kitou, T., Dessert, C., Quiquerez, A., Allemand, P., Lajeunesse, E., 2019. Stream-discharge surges generated by groundwater flow. Geophys. Res. Lett. 46, 7447–7455. https://doi.org/10.1029/2019GL082291. _eprint: https://onlinelibrary.wiley.com/doi/pdf/10.1029/2019GL082291.

Hajj, F., Poszwa, A., Bouchez, J., GuÉrold, F., 2017. Radiogenic and "stable" strontium isotopes in provenance studies: a review and first results on archaeological wood from shipwrecks. J. Archaeol. Sci. 86, 24–49. https://doi.org/10.1016/j.jas.2017.09.005. https://www.sciencedirect.com/science/article/pii/S0305440317301292.

Herndon, E.M., Dere, A.L., Sullivan, P.L., Norris, D., Reynolds, B., Brantley, S.L., 2015. Landscape heterogeneity drives contrasting concentration–discharge relationships in shale headwater catchments. Hydrol. Earth Syst. Sci. 19, 3333–3347. https://doi.org/10.5194/hess-19-3333-2015. https://hess.copernicus.org/articles/19/3333/2015/. publisher: Copernicus GmbH.

Hindshaw, R.S., Tosca, R., Goût, T.L., Farnan, I., Tosca, N.J., Tipper, E.T., 2019. Experimental constraints on Li isotope fractionation during clay formation. Geochim. Cosmochim. Acta 250, 219–237. https://doi.org/10.1016/j.gca.2019.02.015. https://www.sciencedirect.com/science/article/pii/S0016703719300924.

Huh, Y., Chan, L.H., Edmond, J.M., 2001. Lithium isotopes as a probe of weathering processes: Orinoco river. Earth Planet. Sci. Lett. 194, 189–199. https://doi.org/10.1016/S0012-821X(01)00523-4. http://www.sciencedirect.com/science/article/pii/S0012821X01005234.

Inamdar, S.P., O'Leary, N., Mitchell, M.J., Riley, J.T., 2006. The impact of storm events on solute exports from a glaciated forested watershed in western New York, USA. Hydrol. Process. 20, 3423–3439. https://doi.org/10.1002/hyp.6141. _eprint: https://onlinelibrary.wiley.com/doi/pdf/10.1002/hyp.6141.

James, R.H., Palmer, M.R., 2000. The lithium isotope composition of international rock standards. Chem. Geol. 166, 319–326. https://doi.org/10.1016/S0009-2541(99)00217-X. http://www.sciencedirect.com/science/article/pii/S000925419900217X.

Johnson, N.M., Likens, G.E., Bormann, F.H., Fisher, D.W., Pierce, R.S., 1969. A working model for the variation in stream water chemistry at the Hubbard brook experimental forest, New Hampshire. Water Resour. Res. 5, 1353–1363. https://doi.org/10.1029/WR005i006p01353. _eprint: https://onlinelibrary.wiley.com/doi/pdf/10.1029/WR005i006p01353.

Kim, H., Bishop, J.K.B., Dietrich, W.E., Fung, I.Y., 2014. Process dominance shift in solute chemistry as revealed by long-term high-frequency water chemistry observations of groundwater flowing through weathered argillite underlying a steep forested hillslope. Geochim. Cosmochim. Acta 140, 1–19. https://doi.org/10.1016/j.gca.2014.05.011. http://www.sciencedirect.com/science/article/pii/S0016703714003408.

Kim, H., Dietrich, W.E., Thurnhoffer, B.M., Bishop, J.K.B., Fung, I.Y., 2017. Controls on solute concentration-discharge relationships revealed by simultaneous hydrochemistry observations of hillslope runoff and stream flow: the importance of critical zone structure. Water Resour. Res. 53, 1424–1443. https://doi.org/10.1002/2016WR019722. https://agupubs.onlinelibrary.wiley.com/doi/abs/10.1002/2016WR019722.

Kirchner, J.W., 2003. A double paradox in catchment hydrology and geochemistry. Hydrol. Process. 17, 871–874. https://doi.org/10.1002/hyp.5108. _eprint: https://onlinelibrary.wiley.com/doi/pdf/10.1002/hyp.5108.

Knapp, J.L.A., von Freyberg, J., Studer, B., Kiewiet, L., Kirchner, J.W., 2020. Concentration–discharge relationships vary among hydrological events, reflecting differences in event characteristics. Hydrol. Earth Syst. Sci. 24, 2561–2576. https://doi.org/10.5194/hess-24-2561-2020. https://hess.copernicus.org/articles/24/2561/2020/. publisher: Copernicus GmbH.

Koger, J.M., Newman, B.D., Goering, T.J., 2018. Chemostatic behaviour of major ions and contaminants in a semiarid spring and stream system near Los Alamos, NM, USA. Hydrol. Process. 32, 1709–1716. https://doi.org/10.1002/hyp.11624. _eprint: https://onlinelibrary.wiley.com/doi/pdf/10.1002/hyp.11624.

Kurtz, A.C., Lugolobi, F., Salvucci, G., 2011. Germanium-silicon as a flow path tracer: application to the Rio Icacos watershed. Water Resour. Res. 47. https://doi.org/10.1029/2010WR009853. _eprint: https://onlinelibrary.wiley.com/doi/pdf/10.1029/2010WR009853.

Lemarchand, E., Chabaux, F., Vigier, N., Millot, R., Pierret, M.C., 2010. Lithium isotope systematics in a forested granitic catchment (Strengbach, Vosges Mountains, France). Geochim. Cosmochim. Acta 74, 4612–4628. https://doi.org/10.1016/j.gca.2010.04.057. http://www.sciencedirect.com/science/article/pii/S0016703710002425.

Lesack, L.F.W., 1993. Export of nutrients and major ionic solutes from a rain forest catchment in the Central Amazon Basin. Water Resour. Res. 29, 743–758. https://doi.org/10.1029/92WR02372. _eprint: https://onlinelibrary.wiley.com/doi/pdf/10.1029/92WR02372.

Li, W., Liu, X.M., Godfrey, L.V., 2019. Optimisation of lithium chromatography for isotopic analysis in geological reference materials by MC-ICP-MS. Geostand. Geoanal. Res. 43, 261–276. https://doi.org/10.1111/ggr.12254. _eprint: https://onlinelibrary.wiley.com/doi/pdf/10.1111/ggr.12254.

Maher, K., 2011. The role of fluid residence time and topographic scales in determining chemical fluxes from landscapes. Earth Planet. Sci. Lett. 312, 48–58. https://doi.org/10.1016/j.epsl.2011.09.040. http://www.sciencedirect.com/science/article/pii/S0012821X11005607.

McDonnell, J.J., Beven, K., 2014. Debates—the future of hydrological sciences: a (common) path forward? A call to action aimed at understanding velocities, celerities and residence time distributions of the headwater hydrograph. Water Resour. Res. 50, 5342–5350. https://doi.org/10.1002/2013WR015141. _eprint: https://onlinelibrary.wiley.com/doi/pdf/10.1002/2013WR015141.

McGuire, K.J., McDonnell, J.J., 2006. A review and evaluation of catchment transit time modeling. J. Hydrol. 330, 543–563. https://doi.org/10.1016/j.jhydrol.2006.04.020. https://www.sciencedirect.com/science/article/pii/S0022169406002150.

McLaughlin, R.J., Ellen, S., Blake Jr, M., Jayko, A.S., Irwin, W., Aalto, K., Carver, G., Clarke Jr, S., Barnes, J., Cecil, J., 2000. Geology of the Cape Mendocino, Eureka, Garberville, and southwestern part of the Hayfork 30 × 60 minute quadrangles and adjacent offshore area, northern California. U.S. Geological Survey Miscellaneous Field Studies Map MF-2336 1.

Meek, K., Derry, L., Sparks, J., Cathles, L., 2016. ^{87}Sr/^{86}Sr, Ca/Sr, and Ge/Si ratios as tracers of solute sources and biogeochemical cycling at a temperate forested shale catchment, central Pennsylvania, USA. Chem. Geol. 445, 84–102. https://doi.org/10.1016/j.chemgeo.2016.04.026. https://www.sciencedirect.com/science/article/pii/S0009254116302078.

Miller, W.R., Drever, J.I., 1977. Water chemistry of a stream following a storm, Absaroka Mountains, Wyoming. Geol. Soc. Am. Bull. 88, 286–290. https://doi.org/10.1130/0016-7606(1977)88<286:WCOASF>2.0.CO;2.

Millot, R., Guerrot, C., Vigier, N., 2004. Accurate and high-precision measurement of lithium isotopes in two reference materials by MC-ICP-MS. Geostand. Geoanal. Res. 28, 153–159. https://doi.org/10.1111/j.1751-908X.2004.tb01052.x. _eprint: https://onlinelibrary.wiley.com/doi/pdf/10.1111/j.1751-908X.2004.tb01052.x.

Morin, G., France-Lanord, C., Gajurel, A., Gallo, F., Lavé, J., 2014. High K and Ca chemical erosion triggered by physical erosion in a watershed of the high Himalaya of Nepal. Proc. Earth Planet. Sci. 10, 292–296. https://doi.org/10.1016/j.proeps.2014.08.067. https://www.sciencedirect.com/science/article/pii/S1878522014001295.

Mulholland, P.J., Wilson, G.V., Jardine, P.M., 1990. Hydrogeochemical response of a forested watershed to storms: effects of preferential flow along shallow and deep pathways. Water Resour. Res. 26, 3021–3036. https://doi.org/10.1029/WR026i012p03021. _eprint: https://onlinelibrary.wiley.com/doi/pdf/10.1029/WR026i012p03021.

Musolff, A., Schmidt, C., Selle, B., Fleckenstein, J.H., 2015. Catchment controls on solute export. Adv. Water Resour. 86, 133–146. https://doi.org/10.1016/j.advwatres.2015.09.026. https://www.sciencedirect.com/science/article/pii/S030917081500233X.

Nimmo, J.R., Perkins, K.S., Rose, P.E., Rousseau, J.P., Orr, B.R., Twining, B.V., Anderson, S.R., 2002. Kilometer-scale rapid transport of naphthalene sulfonate tracer in the unsaturated zone at the Idaho national engineering and environmental laboratory. Vadose Zone J. 1, 89–101. https://doi.org/10.2113/1.1.89.

Négrel, P., Pauwels, H., Chabaux, F., 2018. Characterizing multiple water-rock interactions in the critical zone through Sr-isotope tracing of surface and groundwater. Appl. Geochem. 93, 102–112. https://doi.org/10.1016/j.apgeochem.2018.04.006. https://www.sciencedirect.com/science/article/pii/S0883292718300908.

Oshun, J., Dietrich, W.E., Dawson, T.E., Fung, I., 2016. Dynamic, structured heterogeneity of water isotopes inside hillslopes. Water Resour. Res. 52, 164–189. https://doi.org/10.1002/2015WR017485. _eprint: https://onlinelibrary.wiley.com/doi/pdf/10.1002/2015WR017485.

Petrone, K.C., Jones, J.B., Hinzman, L.D., Boone, R.D., 2006. Seasonal export of carbon, nitrogen, and major solutes from Alaskan catchments with discontinuous permafrost. J. Geophys. Res., Biogeosci. 111. https://doi.org/10.1029/2005JG000055. _eprint: https://onlinelibrary.wiley.com/doi/pdf/10.1029/2005JG000055.

Pin, C., Bassin, C., 1992. Evaluation of a strontium-specific extraction chromatographic method for isotopic analysis in geological materials. Anal. Chim. Acta 269, 249–255. https://doi.org/10.1016/0003-2670(92)85409-Y. https://www.sciencedirect.com/science/article/pii/000326709285409Y.

Pistiner, J.S., Henderson, G.M., 2003. Lithium-isotope fractionation during continental weathering processes. Earth Planet. Sci. Lett. 214, 327–339. https://doi.org/10.1016/S0012-821X(03)00348-0. http://www.sciencedirect.com/science/article/pii/S0012821X03003480.

PRISM, 2022. PRISM Climate Group. Oregon State University. https://prism.oregonstate.edu/.

Ralph, F.M., Dettinger, M.D., Cairns, M.M., Galarneau, T.J., Eylander, J., 2018. Defining "atmospheric river": how the glossary of meteorology helped resolve a debate. Bull. Am. Meteorol. Soc. 99, 837–839. https://doi.org/10.1175/BAMS-D-17-

0157.1. https://journals.ametsoc.org/view/journals/bams/99/4/bams-d-17-0157.1.
xml, publisher: American Meteorological Society.

Rempe, D.M., Dietrich, W.E., 2018. Direct observations of rock moisture, a hidden component of the hydrologic cycle. Proc. Natl. Acad. Sci. USA 115, 2664–2669. https://doi.org/10.1073/pnas.1800141115. https://www.pnas.org/content/115/11/2664.

Rimon, Y., Dahan, O., Nativ, R., Geyer, S., 2007. Water percolation through the deep vadose zone and groundwater recharge: preliminary results based on a new vadose zone monitoring system. Water Resour. Res. 43. https://doi.org/10.1029/2006WR004855. _eprint: https://onlinelibrary.wiley.com/doi/pdf/10.1029/2006WR004855.

Rose, L.A., Karwan, D.L., Godsey, S.E., 2018. Concentration–discharge relationships describe solute and sediment mobilization, reaction, and transport at event and longer timescales. Hydrol. Process. 32, 2829–2844. https://doi.org/10.1002/hyp.13235. _eprint: https://onlinelibrary.wiley.com/doi/pdf/10.1002/hyp.13235.

Rudnick, R.L., Tomascak, P.B., Njo, H.B., Gardner, L.R., 2004. Extreme lithium isotopic fractionation during continental weathering revealed in saprolites from South Carolina. Chem. Geol. 212, 45–57. https://doi.org/10.1016/j.chemgeo.2004.08.008. http://www.sciencedirect.com/science/article/pii/S0009254104002712.

Ryan, K.A., Adler, T., Chalmers, A., Perdrial, J., Shanley, J.B., Stubbins, A., 2021. Event scale relationships of DOC and TDN fluxes in throughfall and stemflow diverge from stream exports in a forested catchment. J. Geophys. Res., Biogeosci. 126, e2021JG006281. https://doi.org/10.1029/2021JG006281. _eprint: https://onlinelibrary.wiley.com/doi/pdf/10.1029/2021JG006281.

Salve, R., Rempe, D.M., Dietrich, W.E., 2012. Rain, rock moisture dynamics, and the rapid response of perched groundwater in weathered, fractured argillite underlying a steep hillslope. Water Resour. Res. 48. https://doi.org/10.1029/2012WR012583. _eprint: https://agupubs.onlinelibrary.wiley.com/doi/pdf/10.1029/2012WR012583.

Schellekens, J., Scatena, F.N., Bruijnzeel, L.A., van Dijk, A.I.J.M., Groen, M.M.A., van Hogezand, R.J.P., 2004. Stormflow generation in a small rainforest catchment in the Luquillo experimental forest, Puerto Rico. Hydrol. Process. 18, 505–530. https://doi.org/10.1002/hyp.1335. _eprint: https://onlinelibrary.wiley.com/doi/pdf/10.1002/hyp.1335.

Schmidt, L., Rempe, D., 2020. Quantifying dynamic water storage in unsaturated bedrock with borehole nuclear magnetic resonance. Geophys. Res. Lett. 47, e2020GL089600. https://doi.org/10.1029/2020GL089600. _eprint: https://onlinelibrary.wiley.com/doi/pdf/10.1029/2020GL089600.

Sidle, R.C., Tsuboyama, Y., Noguchi, S., Hosoda, I., Fujieda, M., Shimizu, T., 2000. Stormflow generation in steep forested headwaters: a linked hydrogeomorphic paradigm. Hydrol. Process. 14, 369–385. _eprint: https://onlinelibrary.wiley.com/doi/pdf/10.1002/%28SICI%291099-1085%2820000228%2914%3A3%3C369%3A%3AAID-HYP943%3E3.0.CO%3B2-P-2.

Pogge von Strandmann, P.A.E., Porcelli, D., James, R.H., van Calsteren, P., Schaefer, B., Cartwright, I., Reynolds, B.C., Burton, K.W., 2014. Chemical weathering processes in the great Artesian basin: evidence from lithium and silicon isotopes. Earth Planet. Sci. Lett. 406, 24–36. https://doi.org/10.1016/j.epsl.2014.09.014. http://www.sciencedirect.com/science/article/pii/S0012821X1400569X.

Sullivan, P.L., Stops, M.W., Macpherson, G.L., Li, L., Hirmas, D.R., Dodds, W.K., 2019. How landscape heterogeneity governs stream water concentration-discharge be-havior in carbonate terrains (Konza Prairie, USA). Chem. Geol. 527, 118989. https://doi.org/10.1016/j.chemgeo.2018.12.002. https://www.sciencedirect.com/science/article/pii/S0009254118305862.

Thompson, S.E., Basu, N.B., Lascurain Jr., J., Aubeneau, A., Rao, P.S.C., 2011. Relative dominance of hydrologic versus biogeochemical factors on solute export across impact gradients. Water Resour. Res. 47. https://doi.org/10.1029/2010WR009605. _eprint: https://onlinelibrary.wiley.com/doi/pdf/10.1029/2010WR009605.

Torres, M.A., Baronas, J.J., 2021. Modulation of riverine concentration-discharge relationships by changes in the shape of the water transit time distribution. Glob. Biogeochem. Cycles 35, e2020GB006694. https://doi.org/10.1029/2020GB006694. _eprint: https://agupubs.onlinelibrary.wiley.com/doi/pdf/10.1029/2020GB006694.

Tune, A.K., Druhan, J.L., Wang, J., Bennett, P.C., Rempe, D.M., 2020. Carbon dioxide production in bedrock beneath soils substantially contributes to forest carbon cycling. J. Geophys. Res., Biogeosci. 125, e2020JG005795. https://doi.org/10.1029/2020JG005795. _eprint: https://agupubs.onlinelibrary.wiley.com/doi/pdf/10.1029/2020JG005795.

Vigier, N., Decarreau, A., Millot, R., Carignan, J., Petit, S., France-Lanord, C., 2008. Quantifying Li isotope fractionation during smectite formation and implications for the Li cycle. Geochim. Cosmochim. Acta 72, 780–792. https://doi.org/10.1016/j.gca.2007.11.011. http://www.sciencedirect.com/science/article/pii/S0016703707006680.

Wang, J., 2020. Linkages between fluid flow paths, reactive gases, and chemical weathering across a shale bedrock hillslope. Master's thesis. University of Illinois at Urbana-Champaign. http://hdl.handle.net/2142/105930.

Weynell, M., Wiechert, U., Schuessler, J.A., 2017. Lithium isotopes and implications on chemical weathering in the catchment of Lake Donggi Cona, northeastern Tibetan Plateau. Geochim. Cosmochim. Acta 213, 155–177. https://doi.org/10.1016/j.gca.2017.06.026. http://www.sciencedirect.com/science/article/pii/S0016703717303757.

Weynell, M., Wiechert, U., Schuessler, J.A., 2021. Lithium isotope signatures of weathering in the hyper-arid climate of the western Tibetan Plateau. Geochim. Cosmochim. Acta 293, 205–223. https://doi.org/10.1016/j.gca.2020.10.021. https://www.sciencedirect.com/science/article/pii/S0016703720306530.

Williams, L.B., Hervig, R.L., 2005. Lithium and boron isotopes in illite-smectite: the importance of crystal size. Geochim. Cosmochim. Acta 69, 5705–5716. https://doi.org/10.1016/j.gca.2005.08.005. http://www.sciencedirect.com/science/article/pii/S0016703705006058.

Wlostowski, A.N., Gooseff, M.N., McKnight, D.M., Lyons, W.B., 2018. Transit times and rapid chemical equilibrium explain chemostasis in glacial meltwater streams in the McMurdo Dry Valleys, Antarctica. Geophys. Res. Lett. 45, 13,322–13,331. https://doi.org/10.1029/2018GL080369. _eprint: https://onlinelibrary.wiley.com/doi/pdf/10.1029/2018GL080369.

Zhang, X.Y., Saldi, G.D., Schott, J., Bouchez, J., Kuessner, M., Montouillout, V., Henehan, M., Gaillardet, J., 2021. Experimental constraints on Li isotope fractionation during the interaction between kaolinite and seawater. Geochim. Cosmochim. Acta 292, 333–347. https://doi.org/10.1016/j.gca.2020.09.029. https://www.sciencedirect.com/science/article/pii/S0016703720305937.